Ranging sensor fusion in LISA data processing: Treatment of ambiguities, noise, and onboard delays in LISA ranging observables

Jan Niklas Reinhardt,[1,2,*] Martin Staab,[1,2] Kohei Yamamoto,[1,2] Jean-Baptiste Bayle,[3] Aurélien Hees,[4] Olaf Hartwig,[1,2,4] Karsten Wiesner,[1,2] Sweta Shah,[1,2] and Gerhard Heinzel[1,2]

[1]*Max-Planck-Institut für Gravitationsphysik (Albert-Einstein-Institut), Callinstraße 38, 30167 Hannover, Germany*
[2]*Leibniz Universität Hannover, Welfengarten 1, 30167 Hannover, Germany*
[3]*University of Glasgow, Glasgow G12 8QQ, United Kingdom*
[4]*SYRTE, Observatoire de Paris, Université PSL, CNRS, Sorbonne Université, LNE, 61 avenue de l'observatoire 75014 Paris, France*

(Received 11 July 2023; accepted 29 November 2023; published 10 January 2024)

Interspacecraft ranging is crucial for the suppression of laser frequency noise via time-delay interferometry (TDI). So far, the effects of onboard delays and ambiguities on the Laser Interferometer Space Antenna (LISA) ranging observables were neglected in LISA modeling and data processing investigations. In reality, onboard delays cause offsets and timestamping delays in the LISA measurements, and pseudorandom noise (PRN) ranging is ambiguous, as it determines only the range up to an integer multiple of the PRN code length. In this article, we identify the four LISA ranging observables: PRN ranging, the sideband beat notes at the interspacecraft interferometer, TDI ranging, and ground-based observations. We derive their observation equations in the presence of onboard delays, noise, and ambiguities. We then propose a three-stage ranging sensor fusion to combine these observables in order to gain accurate and precise ranging estimates. We propose to calibrate the onboard delays on ground and to compensate the associated offsets and timestamping delays in an initial data treatment (stage 1). We identify the ranging-related routines, which need to run continuously during operation (stage 2) and implement them numerically. Essentially, this involves the reduction of ranging noise, for which we develop a Kalman filter combining the PRN ranging and the sideband beat notes. We further implement cross-checks for the PRN ranging ambiguities and offsets (stage 3). We show that both ground-based observations and TDI ranging can be used to resolve the PRN ranging ambiguities. Moreover, we apply TDI ranging to estimate the PRN ranging offsets.

DOI: 10.1103/PhysRevD.109.022004

I. INTRODUCTION

The Laser Interferometer Space Antenna (LISA), due for launch around the year 2035, is an ESA-led mission for space-based gravitational-wave detection in the frequency band between 0.1 mHz and 1 Hz [1]. LISA consists of three satellites forming an approximate equilateral triangle with an arm length of 2.5 Gm, in a heliocentric orbit that trails or leads Earth by about 20°. Six infrared laser links with a nominal wavelength of 1064 nm connect the three spacecraft (SC), whose relative motion necessitates the usage of heterodyne interferometry. Phasemeters are used to extract the phases of the corresponding beat notes [2], in which gravitational waves manifest in form of microcycle deviations equivalent to picometer variations in the interspacecraft ranges.

The phasemeter output, however, is obscured by various instrumental noise sources. They must be suppressed to fit in the LISA noise budget of 10 pm $\mathrm{Hz}^{-0.5}$ (single link); otherwise, they would bury the gravitational-wave signals. Dedicated data-processing algorithms are being developed for each of these instrumental noise sources; their subsequent execution is referred to as initial noise reduction pipeline (INReP). The dominating noise source in LISA is by far the laser frequency noise, which must be reduced by more than 8 orders of magnitude. This is achieved by time-delay interferometry (TDI), which combines the various beat notes with the correct delays to virtually form equal-optical-path-length interferometers, in which laser frequency noise naturally cancels [3,4]. The exact definition

*janniklas.reinhardt@aei.mpg.de

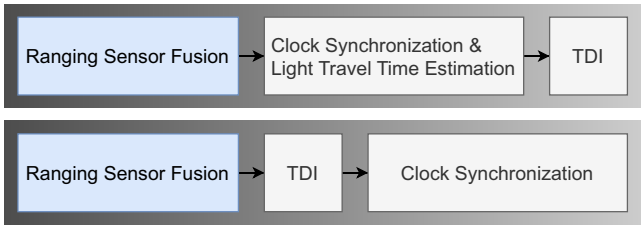

FIG. 1. In the baseline TDI topology (upper part), we perform TDI after clock synchronization to TCB; the delays are given by the light travel times. In the alternative TDI topology (lower part), we execute TDI without clock synchronization and apply the pseudoranges as delays [5]. Both topologies rely on a ranging sensor fusion.

of these delays depends on the location of TDI within the INReP (see Fig. 1) [5], but, wherever we place it, some kind of information about the absolute interspacecraft ranges is required.

Yet, absolute ranges are not a natural signal in a continuous-wave heterodyne laser interferometer such as LISA. Therefore, a ranging scheme based on pseudorandom noise (PRN) codes is implemented [6–8]: Each SC houses a free-running ultrastable oscillator (USO) as a timing reference. It defines the spacecraft elapsed time (SCET). PRN codes generated according to the respective SCETs are imprinted onto the laser beams by phase modulating the carrier. The comparison of a PRN code received from a distant SC, hence generated according to the distant SCET, with a local copy enables a measurement of the pseudorange: The pseudorange is commonly defined as the difference between the SCET of the receiving SC at the event of reception and the SCET of the emitting SC at the event of emission [9]. It represents a combination of the true geometrical range (light travel time) with the offset between the two involved SCETs [see Eq. (A5)].

In the baseline TDI topology (upper row in Fig. 1), TDI is performed after SCET synchronization to the barycentric coordinate time (TCB); the light travel times are used as delays. The pseudoranges comprise information about both the light travel times and the SCET offsets required for synchronizing the clocks (see Appendix A). A Kalman filter can be used to disentangle the pseudoranges in order to retrieve light travel times and SCET offsets [10]. In the alternative TDI topology (lower row in Fig. 1), the pseudoranges are directly used as delays. In that topology, TDI is executed on the unsynchronized beat notes sampled according to the respective SCETs [5].

However, PRN ranging (PRNR) does not directly provide the pseudoranges but requires three treatments. First, due to the finite PRN code length (we assume 400 km), PRNR measures the pseudoranges modulo an ambiguity [6]. Second, onboard delays due to signal propagation and processing cause offsets and timestamping delays in the PRNR. Third, PRNR is limited by white ranging noise with an rms amplitude of about 0.3 m, which is due to shot noise and PRN code interference [8,11]. To overcome these difficulties, there are three additional pseudorange observables, which are actually designed for other purposes and serve that function secondarily: Ground-based observations provide inaccurate but unambiguous pseudorange estimates; time-delay interferometric ranging (TDIR) turns TDI upside down seeking a model for the delays that minimizes the laser frequency noise in the TDI combinations [12]; the sideband beat notes, primarily designed for clock noise correction, provide a measurement of the pseudorange time derivatives [5]. The combination of these four observables in order to form optimal pseudorange estimates is referred to as *ranging sensor fusion* in the course of this article. It is common to both TDI topologies (see Fig. 1) and, consequently, a crucial stage of the INReP.

In Sec. II, we specify the pseudorange definition in the context of onboard delays and identify the delays required for TDI. We then derive observation equations for the four pseudorange observables in Sec. III. Here, we carefully consider the effects of onboard delays at the interspacecraft interferometer.[1] In Sec. IV, we introduce a three-stage ranging sensor fusion consisting of an initial data treatment, a core ranging processing, and cross-checks. In the initial data treatment, we propose to compensate for the offsets and timestamping delays caused by the onboard delays. We identify PRNR unwrapping and noise reduction as the ranging processing steps that need to run continuously during operation. In parallel to this core ranging processing, we propose cross-checks of the PRNR ambiguities and offsets. We implement the core ranging processing and the cross-checks numerically. In Sec. V, we discuss the performance of this implementation and conclude in Sec. VI.

II. THE PSEUDORANGE AND TDI IN THE CONTEXT OF ONBOARD DELAYS

A. Brief description of the LISA payload

Each SC houses an ultrastable oscillator (USO) generating a signal at about 50 MHz. An 80 MHz clock signal, the phasemeter clock (PMC), is coherently derived from this USO. The PMC can be considered as the timing reference on board the SC (see Fig. 4), and its associated counter is referred to as spacecraft elapsed time:

$$\mathrm{SCET}(n) = \sum_{1}^{n} \frac{1}{80\ \mathrm{MHz}}. \tag{1}$$

It is useful to consider the SCET as a continuous timescale, which we denote by $\hat{\tau}$. It differs from the barycentric coordinate time (TCB), denoted by t, due to instrumental clock drifts and jitters and due to relativistic effects.

[1]We neglect such delays for the reference and test-mass interferometers, which we will treat in a follow-up work.

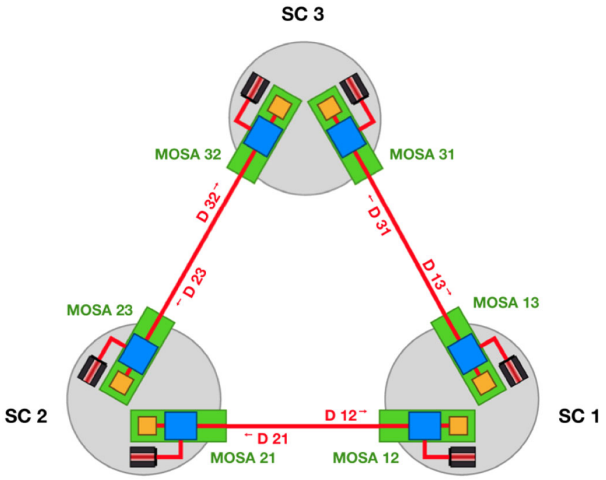

FIG. 2. LISA labeling conventions (from [14]). The SC are labeled clockwise. The MOSAs and their associated building blocks (lasers, interferometers, etc.) are labeled by two indices: the first one indicates the SC they are located at and the second one the SC they are oriented to. The measurements and related quantities (optical links, pseudoranges, etc.) share the indices of the MOSAs they are measured at. Below, we distinguish between left-handed MOSAs (12, 23, and 31) and right-handed ones (13, 32, and 21).

Following the notation of [13], we use superscripts to indicate a quantity to be expressed as function of a certain time scale; e.g., $\hat{\tau}_1^t$ denotes the SCET of SC 1 as a function of the TCB. Note that

$$\hat{\tau}_i^{\hat{\tau}_i}(\tau) = \tau. \tag{2}$$

Each SC contains two movable optical subassemblies (MOSAs) connected by an optical fiber (see Fig. 2 for the labeling conventions). Each MOSA has an associated laser and houses a telescope, a free-falling test mass marking the end of the corresponding optical link, and an optical bench with three interferometers: the interspacecraft interferometer (ISI), in which the gravitational-wave signals eventually appear, the reference interferometer (RFI) to compare local and adjacent lasers, and the test-mass interferometer (TMI) to sense the optical bench motion with respect to the free-falling test mass in direction of the optical link. The MHz beat notes in these interferometers are detected with quadrant photoreceivers (QPRs). They are digitized in analog-to-digital converters (ADCs) driven by the PMCs. Phasemeters extract the beat note phases[2] using digital phase-locked loops (DPLLs). These phases are then downsampled to 4 Hz in a multistage decimation procedure (DEC) and telemetered to Earth (see Fig. 4).

[2]Within the phasemeter, both phase and frequency exist numerically. In the current design, the phasemeters deliver the beat note frequencies with occasional phase anchor points.

B. The pseudorange and onboard delays

The pseudorange, denoted by $R_{ij}^{\hat{\tau}_i}$, is commonly defined as the difference between the SCET of the receiving SC at the event of reception and the SCET of the emitting SC at the event of emission [9]. It represents a combination of the light travel time between the emission at SC j and the reception at SC i and the differential SCET offset [see Eq. (A5)]. However, considering the complexity of the LISA metrology system, this definition appears to be rather vague: To what exactly do we relate the events of emission and reception? Two specifications are required here: We need to locate emission and reception, and we need to define the actual events.

It is convenient to consider emission and reception at the respective polarizing beam splitters (PBSs) in front of the telescopes (denoted PBS1 in [15]) and to treat the onboard signal propagation and processing on both SC as onboard delays (see Fig. 3). Thus, we clearly separate the pseudorange from onboard delays. Note that this definition is not unique; the events of emission and reception could be located elsewhere, assuming that the onboard delays are defined accordingly.

The LISA optical links do not involve delta-pulse-like events. In order to define the actual events of emission and reception, we, instead, use the instants when the light phase changes at the beginning of the first PRN code chip. At first glance, the PRN code might seem unfavorable for the pseudorange definition, as PRN and carrier phase are oppositely affected by the solar wind: The PRN phase is delayed by the group delay, while the carrier phase is advanced by the phase delay. However, these effects are at the order of 10 pm (see Appendix C), whereas our best pseudorange estimates are at 0.1 mm accuracy. Consequently, the solar wind dispersion can be neglected in the pseudorange definition.

When expressing the interferometric measurements according to this specified pseudorange definition, we need to consider the excluded onboard signal propagation and processing. For that purpose, we introduce two kinds of delay operators by their action on a function $f^{\hat{\tau}_j}$. The onboard delay operator describes delays due to onboard signal propagation and processing and is defined on the same SCET as the function it is acting on:

$$\mathbf{D}_x^{\hat{\tau}_j} f^{\hat{\tau}_j}(\tau) = f^{\hat{\tau}_j}\left(\tau - d_x^{\hat{\tau}_j}(\tau)\right). \tag{3}$$

x is a place holder for any onboard delay, e.g., $\mathbf{D}_{\mathrm{qpr}\leftarrow\mathrm{pbs}}$ denotes the optical path length from the PBS to the QPR and $\mathbf{D}_{\mathrm{dec}}$ the decimation filter group delay. The interspacecraft delay operator is defined on a different SCET than the function it is acting on and applies the pseudorange as delay:

$$\mathbf{D}_{ij}^{\hat{\tau}_i} f^{\hat{\tau}_j}(\tau) = f^{\hat{\tau}_j}\left(\tau - R_{ij}^{\hat{\tau}_i}(\tau)\right). \tag{4}$$

For onboard delays that differ between carrier, PRN, and sideband signals, we add the superscripts *car*, *prn*, and *sb*, respectively. To trace the full path of a signal from the distant SC, we need to combine the interspacecraft delay operator for the interspacecraft signal propagation and the SCET conversion (considered at the PBS of the receiving SC) with onboard delay operators on both SC. The application of a delay operator to another time-dependent delay operator results in nested delays:

$$\mathbf{D}_x^{\hat{\tau}_i}\mathbf{D}_{ij}^{\hat{\tau}_i} f^{\hat{\tau}_j}(\tau) = f^{\hat{\tau}_j}\left(\tau - d_x^{\hat{\tau}_i}(\tau) - R_{ij}^{\hat{\tau}_i}\left(\tau - d_x^{\hat{\tau}_i}(\tau)\right)\right). \tag{5}$$

For a constant delay operator $\mathbf{D}_x$, we can define the associated advancement operator $\mathbf{A}_x$ acting as its inverse:

$$\mathbf{A}_x^{\hat{\tau}_j} f^{\hat{\tau}_j}(\tau) = f^{\hat{\tau}_j}\left(\tau + d_x^{\hat{\tau}_j}\right), \tag{6}$$

$$\mathbf{A}_x\mathbf{D}_x f^{\hat{\tau}_j}(\tau) = f^{\hat{\tau}_j}\left(\tau - d_x^{\hat{\tau}_j} + d_x^{\hat{\tau}_j}\right) = f^{\hat{\tau}_j}(\tau). \tag{7}$$

For advancement operators associated to propagation delays, we write

$$\mathbf{D}^{-1}_{\text{qpr}\leftarrow\text{pbs}} = \mathbf{A}_{\text{pbs}\leftarrow\text{qpr}}, \tag{8}$$

where the subscript underlines that the advancement operator undoes the signal propagation. Below, we consider onboard delays as constant or slowly time varying so that their associated advancement operators are well defined.

C. Delays for TDI

In [5] the pseudoranges are identified as the delays that need to be applied to cancel the laser noise in the alternative TDI topology (see Fig. 1). Does this statement hold in the presence of onboard delays considering the refined pseudorange definition in Sec. II B? To identify the delays $\mathcal{D}_{ij}^{\hat{\tau}_i}$ that are required in TDI combinations to suppress the laser noise, let us set up a simple TDI toy model: We consider the two MOSAs depicted in Fig. 3 and the TDI combination, where we combine $\text{ISI}_{21}^{\hat{\tau}_2}$ with $\text{ISI}_{12}^{\hat{\tau}_1}$ delayed by $\mathcal{D}_{21}^{\hat{\tau}_2}$. We will identify the expression of $\mathcal{D}_{21}^{\hat{\tau}_2}$, which leads to a suppression of the noise from laser 12.

Let us first define the delays that are at play in this situation and highlighted in Fig. 3. We denote the delay that is common to both the local and the outgoing beam by $\mathbf{D}_{\text{A}}^{\hat{\tau}_1}$. It corresponds to the path from the laser source to the beam splitter (BS), which divides them (denoted BS2 in [15]). The delays associated to the paths traversed only by the local and the outgoing beam are called $\mathbf{D}_{\text{B}}^{\hat{\tau}_1}$ and $\mathbf{D}_{\text{C}}^{\hat{\tau}_2}$. Note that they represent combinations of the delays from the BS

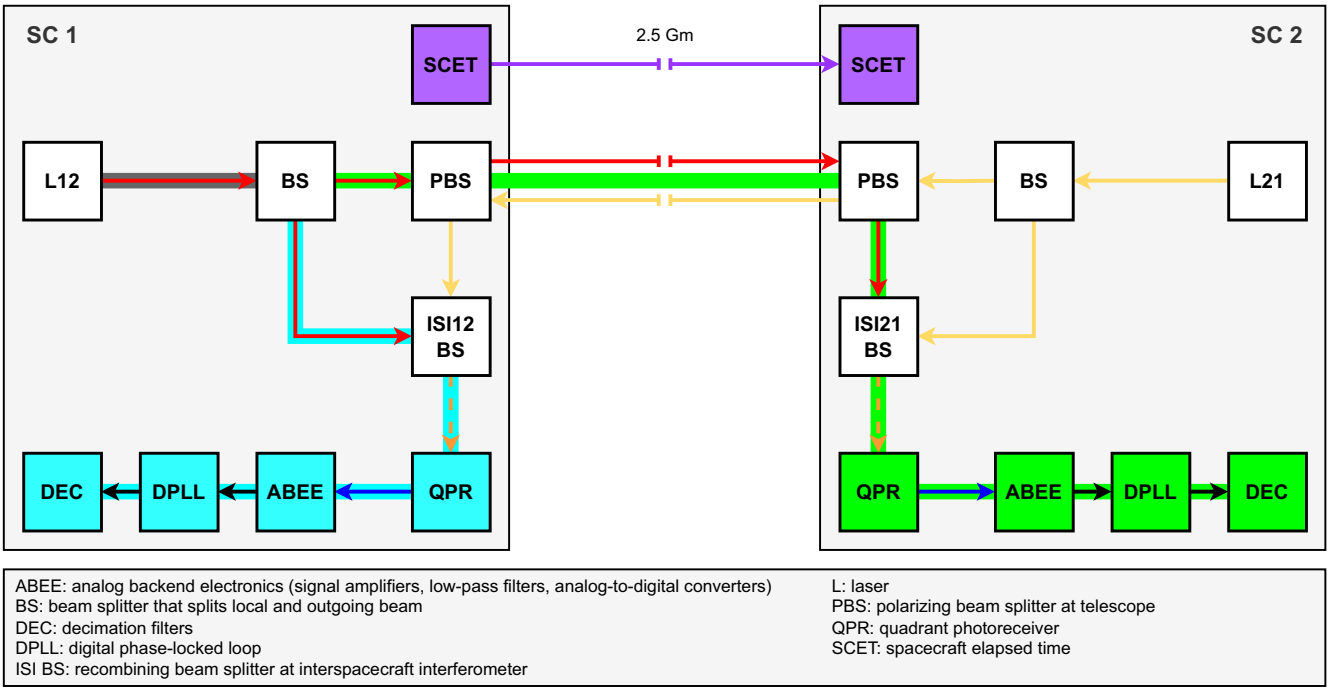

FIG. 3. We trace laser 12 (red arrows) and laser 21 (yellow arrows) to the ISI BSs on both SC, where they interfere and form beat notes (orange dashed arrows). In the subsequent data processing chain, we indicate analog signals by blue and digital signals by black arrows. Constituents of the pseudorange are marked purple. These are the light travel time between the PBSs (at the telescopes) and the transformation between the two SCETs. In Sec. II C, we identify the TDI delay that is required to cancel the noise of laser 12. For that purpose, we mark the common path of the outgoing and the local beam in dark gray, the noncommon path of the local beam in light blue, and the noncommon path of the outgoing beam in green.

to the recombining beam splitters at the respective interspacecraft interferometers (ISI BSs) (denoted BS12 in [15]), where the measurements are formed, with delays from the ISI BSs to the decimation filters, where the measurements are timestamped. Moreover, $\mathbf{D}_{\mathrm{C}}^{\hat{\tau}_2}$ combines an interspacecraft delay operator with onboard delays on both SC. Accordingly, we define the delays $\mathbf{D}_{\mathrm{A}}^{\hat{\tau}_2}$, $\mathbf{D}_{\mathrm{B}}^{\hat{\tau}_2}$, and $\mathbf{D}_{\mathrm{C}}^{\hat{\tau}_1}$ for laser 21.

Now the TDI delay $\mathcal{D}_{21}^{\hat{\tau}_2}$ can be derived as

$$\mathcal{D}_{21}^{\hat{\tau}_2}\mathrm{ISI}_{12}^{\hat{\tau}_1}(\tau)+\mathrm{ISI}_{21}^{\hat{\tau}_2}(\tau) \tag{9}$$

$$=\mathcal{D}_{21}^{\hat{\tau}_2}\left(\mathbf{D}_{\mathrm{C}}^{\hat{\tau}_1}\mathbf{D}_{\mathrm{A}}^{\hat{\tau}_2}\Phi_{21}^{\hat{\tau}_2}(\tau)-\mathbf{D}_{\mathrm{B}}^{\hat{\tau}_1}\mathbf{D}_{\mathrm{A}}^{\hat{\tau}_1}\Phi_{12}^{\hat{\tau}_1}(\tau)\right)+\mathbf{D}_{\mathrm{C}}^{\hat{\tau}_2}\mathbf{D}_{\mathrm{A}}^{\hat{\tau}_1}\Phi_{12}^{\hat{\tau}_1}(\tau)-\mathbf{D}_{\mathrm{B}}^{\hat{\tau}_2}\mathbf{D}_{\mathrm{A}}^{\hat{\tau}_2}\Phi_{21}^{\hat{\tau}_2}(\tau) \tag{10}$$

$$=\left(\mathbf{D}_{\mathrm{C}}^{\hat{\tau}_2}-\mathcal{D}_{21}^{\hat{\tau}_2}\mathbf{D}_{\mathrm{B}}^{\hat{\tau}_1}\right)\mathbf{D}_{\mathrm{A}}^{\hat{\tau}_1}\Phi_{12}^{\hat{\tau}_1}(\tau)+(\cdots)\Phi_{21}^{\hat{\tau}_2}(\tau), \tag{11}$$

where $\Phi_{12}^{\hat{\tau}_1}$ denotes the phase of laser 12. In the second step, we factor out the common delay $\mathbf{D}_{\mathrm{A}}^{\hat{\tau}_1}$, which does not contribute to the TDI delay $\mathcal{D}_{21}^{\hat{\tau}_2}$. We ignore the phase $\Phi_{21}^{\hat{\tau}_2}$ of laser 21, as we focus on canceling the noise of laser 12. For that purpose, we need to choose the delay $\mathcal{D}_{21}^{\hat{\tau}_2}$, such that the first bracket vanishes, i.e.,

$$\mathcal{D}_{21}^{\hat{\tau}_2}=\mathbf{D}_{\mathrm{C}}^{\hat{\tau}_2}(\mathbf{D}_{\mathrm{B}}^{-1})^{\hat{\tau}_1}=\mathbf{D}_{\mathrm{C}}^{\hat{\tau}_2}\mathbf{A}_{\mathrm{B}}^{\hat{\tau}_1} \tag{12}$$

$$=\mathbf{D}_{\mathrm{dec}\leftarrow\mathrm{qpr}}^{\hat{\tau}_2}\mathbf{D}_{\mathrm{qpr}\leftarrow\mathrm{pbs}}^{\hat{\tau}_2}\mathbf{D}_{21}^{\hat{\tau}_2}\mathbf{D}_{\mathrm{pbs}\leftarrow\mathrm{bs}}^{\hat{\tau}_1}\mathbf{A}_{\mathrm{bs}\leftarrow\mathrm{qpr}}^{\hat{\tau}_1}\mathbf{A}_{\mathrm{qpr}\leftarrow\mathrm{dec}}^{\hat{\tau}_1}. \tag{13}$$

The advancement operators are associated to the noncommon path of the local beam, the delay operators to the noncommon path of the outgoing beam. Hence, to cancel the noise of laser 12, we need to consider the difference between the delays applied to laser 12 in the ISI measurements on SC 1 and SC 2.

The TDI delays $\mathcal{D}_{ij}^{\hat{\tau}_i}$ represent combinations of interspacecraft delay operators (pseudoranges) with onboard delay and advancement operators on both SC. We propose to calibrate all required onboard delays on ground before mission start and to measure the pseudorange during operation. The next section covers the four pseudorange observables. Before, we close this section with a few remarks on the required onboard delays. $\mathbf{D}_{\mathrm{pbs}\leftarrow\mathrm{bs}}^{\hat{\tau}_1}$ and $\mathbf{D}_{\mathrm{qpr}\leftarrow\mathrm{pbs}}^{\hat{\tau}_2}$ are small optical path length delays of the outgoing beam before transmission and after reception at the distant SC. $\mathbf{A}_{\mathrm{bs}\leftarrow\mathrm{qpr}}^{\hat{\tau}_1}$ is a small optical path length advancement of the local beam. These optical path lengths are on the order of 10 cm to 1 m [15]. $\mathbf{D}_{\mathrm{dec}\leftarrow\mathrm{qpr}}^{\hat{\tau}_2}$ is the signal processing delay on the receiving SC. $\mathbf{A}_{\mathrm{qpr}\leftarrow\mathrm{dec}}^{\hat{\tau}_1}$ is the corresponding advancement on the local SC. It can be decomposed into

$$\mathbf{D}_{\mathrm{dec}\leftarrow\mathrm{qpr}}=\mathbf{D}_{\mathrm{dec}}^{\mathrm{car}}\mathbf{D}_{\mathrm{dpll}}^{\mathrm{car}}\mathbf{D}_{\mathrm{dpll}\leftarrow\mathrm{abee}}\mathbf{D}_{\mathrm{abee}}^{\mathrm{car}}\mathbf{D}_{\mathrm{abee}\leftarrow\mathrm{qpr}}\mathbf{D}_{\mathrm{qpr}}^{\mathrm{car}}. \tag{14}$$

The group delays of the quadrant photoreceiver $\mathbf{D}_{\mathrm{qpr}}^{\mathrm{car}}$ and the analog back-end electronics $\mathbf{D}_{\mathrm{abee}}^{\mathrm{car}}$ depend among others on the beat note frequency [16]. Hence, they change over time and differ between carrier, sideband, and PRN signals. Together with the cable delays $\mathbf{D}_{\mathrm{abee}\leftarrow\mathrm{qpr}}$ and $\mathbf{D}_{\mathrm{dpll}\leftarrow\mathrm{abee}}$, they can amount to 10 m. The DPLL delay $\mathbf{D}_{\mathrm{dpll}}^{\mathrm{car}}$ depends on the time-dependent beat note amplitude [2,11]. All time-dependent contributions should be calibrated for all combinations of the time-dependent parameters. Hence, during operation they can be constructed with the help of SC monitors providing the corresponding parameter values, e.g., beat note frequency and amplitude.

III. RANGING MEASUREMENTS

A. PRN ranging (PRNR)

PRNR is the onboard ranging scheme in LISA. A set of six PRN sequences has been computed such that the cross-correlations and the autocorrelations for nonzero delays are minimized. These PRN codes are associated to the six optical links in the LISA constellation. The PRN codes are generated according to the respective PMCs and imprinted onto the laser beams by phase modulating the carriers in electro-optical modulators (EOMs) (see Fig. 4). In each phasemeter, DPLLs are applied to extract the beat note phases. The PRN codes show up in the DPLL error signals, since the DPLL bandwidth of 10 to 100 kHz is lower than the PRN chipping rate of about 1 MHz. In a delay-locked loop (DLL), these error signals are correlated with PRN codes generated according to the local SCET. The local delay that maximizes the correlation yields a pseudorange measurement: the PRNR [6,7].

We now derive the PRNR observation equation carefully taking into account onboard delays. We model the path of the PRN code from the distant SC to the local DLL by applying delay operators to the distant SCET:

$$\mathbf{D}_{\mathrm{dll}\leftarrow\mathrm{pbs}}^{\mathrm{prn},\hat{\tau}_i}\mathbf{D}_{ij}^{\hat{\tau}_i}\mathbf{D}_{\mathrm{pbs}\leftarrow\mathrm{pmc}}^{\mathrm{pm},\hat{\tau}_j}\hat{\tau}_j^{\hat{\tau}_j}(\tau). \tag{15}$$

The two onboard delays can be decomposed into

$$\mathbf{D}_{\mathrm{pbs}\leftarrow\mathrm{pmc}}^{\mathrm{prn}}=\mathbf{D}_{\mathrm{pbs}\leftarrow\mathrm{eom}}\mathbf{D}_{\mathrm{eom}\leftarrow\mathrm{prn}}\mathbf{D}_{\mathrm{pm}}\mathbf{D}_{\mathrm{prn}\leftarrow\mathrm{pmc}}, \tag{16}$$

$$\mathbf{D}_{\mathrm{dll}\leftarrow\mathrm{pbs}}^{\mathrm{prn}}=\mathbf{D}_{\mathrm{dll}}\mathbf{D}_{\mathrm{dpll}}^{\mathrm{prn}}\mathbf{D}_{\mathrm{dpll}\leftarrow\mathrm{abee}}\mathbf{D}_{\mathrm{abee}}^{\mathrm{prn}}\mathbf{D}_{\mathrm{abee}\leftarrow\mathrm{qpr}}\mathbf{D}_{\mathrm{qpr}}^{\mathrm{prn}}\mathbf{D}_{\mathrm{qpr}\leftarrow\mathrm{pbs}}. \tag{17}$$

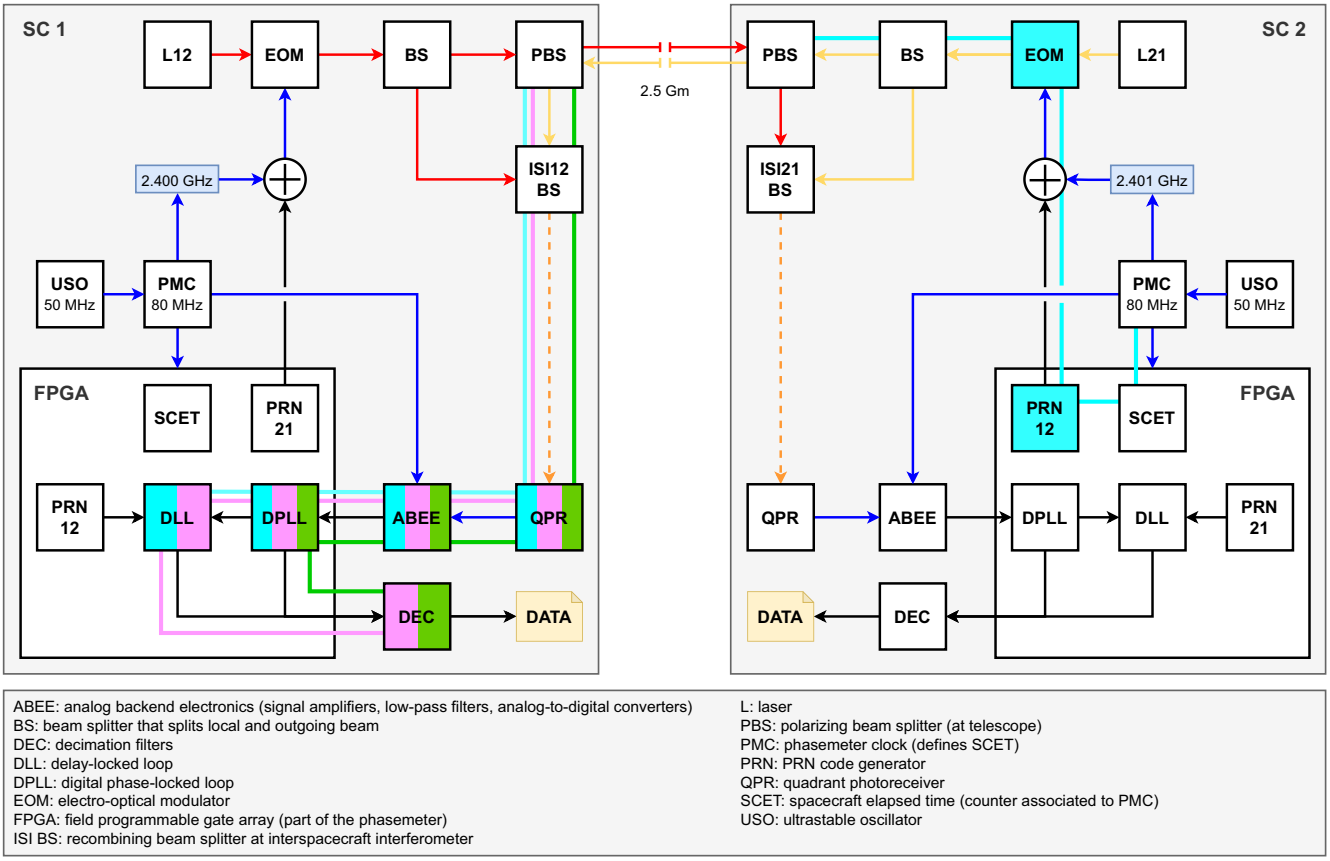

FIG. 4. We revisit Fig. 3. Again, we trace the lasers 12 and 21 to the ISI BSs, where they interfere and form beat notes. The carriers are phase modulated with the GHz clock and the PRN signals (follow the arrows from the PMC and the PRN to the EOM). Blue arrows indicate analog signals and black arrows digital ones. We show the USO frequency distribution (follow the arrows after the USOs) and illustrate the onboard signal processing (follow the arrows after the QPRs). We highlight the timestamping delays and offsets in the pseudorange observables caused by onboard delays. In light blue, we mark the PRNR offset from the pseudorange. The PRNR timestamping delay is drawn pink; the sideband timestamping delay is marked green.

$\mathbf{D}^{\mathrm{prn}}_{\mathrm{pbs}\leftarrow\mathrm{pmc}}$ consists of the cable delays from the PMC to the EOM, the processing delay due to the PRN code generation, and the optical path length from the EOM to the PBS. All these delays are constant at the sensitive scale of PRNR, so that we do not have to consider delay nesting in $\mathbf{D}^{\mathrm{prn}}_{\mathrm{pbs}\leftarrow\mathrm{pmc}}$. We added the superscript *prn* because this path is different for the sideband signal (see Fig. 4). $\mathbf{D}^{\mathrm{prn}}_{\mathrm{dll}\leftarrow\mathrm{pbs}}$ is explained in the next paragraph as part of the PRNR timestamping delay. At the DLL, the received PRN codes are correlated with identical codes generated according to the local SCET. We model this correlation as the difference between the local SCET and the delayed distant SCET [Eq. (15)], and we apply $\mathbf{D}^{\mathrm{prn}}_{\mathrm{dec}}$ to model the group delay of the decimation filters applicable to PRN ranging:

$$\mathbf{D}^{\mathrm{prn}}_{\mathrm{dec}}\left(\hat{\tau}^{\hat{\tau}_i}_i(\tau)-\mathbf{D}^{\mathrm{prn},\hat{\tau}_i}_{\mathrm{dll}\leftarrow\mathrm{pbs}}\mathbf{D}^{\hat{\tau}_i}_{ij}\mathbf{D}^{\mathrm{prn},\hat{\tau}_j}_{\mathrm{pbs}\leftarrow\mathrm{pmc}}\hat{\tau}^{\hat{\tau}_j}_j(\tau)\right). \tag{18}$$

To see how the onboard delays affect the PRNR, we expand Eq. (18) by applying Eq. (2):

$$\begin{aligned}&\mathbf{D}^{\mathrm{prn}}_{\mathrm{dec}}\left(\hat{\tau}^{\hat{\tau}_i}_i(\tau)-\hat{\tau}^{\hat{\tau}_j}_j\left(\tau-d^{\hat{\tau}_i}_{\mathrm{dll}\leftarrow\mathrm{pbs}}-R^{\hat{\tau}_i}_{ij}\left(\tau-d^{\hat{\tau}_i}_{\mathrm{dll}\leftarrow\mathrm{pbs}}\right)\right.\right.\\&\quad\left.\left.-d^{\hat{\tau}_j}_{\mathrm{pbs}\leftarrow\mathrm{pmc}}\right)\right)\\&=\mathbf{D}^{\mathrm{prn},\hat{\tau}_i}_{\mathrm{dec}\leftarrow\mathrm{pbs}}R^{\hat{\tau}_i}_{ij}(\tau)+O^{\mathrm{prn}}_{ij}\,.\end{aligned} \tag{19}$$

The onboard delays cause the PRNR timestamping delay $\mathbf{D}^{\mathrm{prn}}_{\mathrm{dec}\leftarrow\mathrm{pbs}}$ and the PRNR offset O^{prn}_{ij}:

$$\begin{aligned}\mathbf{D}^{\mathrm{prn}}_{\mathrm{dec}\leftarrow\mathrm{pbs}}=\mathbf{D}^{\mathrm{prn}}_{\mathrm{dec}}\mathbf{D}_{\mathrm{dll}}\mathbf{D}^{\mathrm{prn}}_{\mathrm{dpll}}\mathbf{D}_{\mathrm{dpll}\leftarrow\mathrm{abee}}\mathbf{D}^{\mathrm{prn}}_{\mathrm{abee}}\\\mathbf{D}_{\mathrm{abee}\leftarrow\mathrm{qpr}}\mathbf{D}^{\mathrm{prn}}_{\mathrm{qpr}}\mathbf{D}_{\mathrm{qpr}\leftarrow\mathrm{pbs}},\end{aligned} \tag{20}$$

$$O^{\mathrm{prn}}_{ij}=d^{\hat{\tau}_i}_{\mathrm{dll}\leftarrow\mathrm{pbs}}+d^{\hat{\tau}_j}_{\mathrm{pbs}\leftarrow\mathrm{pmc}}. \tag{21}$$

The PRNR timestamping delay has similar constituents as the onboard delays appearing in the TDI delay $\mathcal{D}_{ij}$; they are marked pink in Fig. 4. However, most of them are frequency or amplitude dependent. Therefore, they differ between carrier and PRN signals. As for the TDI delay, we propose

to individually calibrate all constituents of the PRNR timestamping delay on ground before mission start. Hence, during operation $\mathbf{D}^{\mathrm{prn}}_{\mathrm{dec}\leftarrow\mathrm{pbs}}$ can be compensated in an initial data treatment by application of its associated advancement operator $\mathbf{A}^{\mathrm{prn}}_{\mathrm{pbs}\leftarrow\mathrm{dec}}$. After that, the PRNR observation equation including ranging noise and PRN ambiguity can be written as

$$\mathbf{A}^{\mathrm{prn},\hat{\tau}_i}_{\mathrm{pbs}\leftarrow\mathrm{dec}}\mathrm{PRNR}^{\hat{\tau}_i}_{ij}(\tau) = R^{\hat{\tau}_i}_{ij}(\tau) + O^{\mathrm{prn}}_{ij} + N^{\mathrm{prn}}_{ij}(\tau) - a^{\mathrm{prn}}_{ij}(\tau)\cdot l. \tag{22}$$

l denotes the finite PRN code length. We use 400 km as a placeholder; the final value has not been decided. The finite PRN code length leads to an ambiguity; a^{prn}_{ij} denote the associated ambiguity integers [7]. N^{prn}_{ij} is the white ranging noise with an rms amplitude of about 0.3 m at the 4 Hz data rate, which is due to shot noise and PRN code interference [8,11]. The latter refers to the interference between the PRN code modulated onto the received laser at the distant SC and the other code modulated onto the local laser at the local SC. The PRNR offset O^{prn}_{ij} involves contributions on the emitter and on the receiver side [see Eq. (21)]; they are marked light blue in Fig. 4. It can amount to 10 m and more [11,17]. Similar to the PRNR timestamping delay, we propose to calibrate the PRNR offset on ground, so that it can be subtracted in an initial data treatment.

B. Sideband ranging (SBR)

For the purpose of in-band clock noise correction in the INReP, a clock noise transfer between the SC is implemented [8]: The 80 MHz PMC signals are up-converted to $\nu^{\mathrm{m}}_l = 2.400$ GHz and $\nu^{\mathrm{m}}_r = 2.401$ GHz for left- and right-handed MOSAs, respectively (see Fig. 2 for the definition of left- and right-handed MOSAs). The EOMs phase-modulate the carriers with the up-converted PMC signals, thereby creating clock sidebands. We show below that the beat notes between these clock sidebands constitute a pseudorange observable.

Considering onboard delays, the difference between carrier and sideband beat notes can be written as

$$\begin{aligned}\mathrm{ISI}^{\hat{\tau}_i}_{ij}(\tau) - \mathrm{ISI}^{\hat{\tau}_i}_{\mathrm{sb},ij}(\tau) = -\mathbf{D}^{\mathrm{sb},\hat{\tau}_i}_{\mathrm{dec}\leftarrow\mathrm{isi\ bs}}\Bigg\{&\mathbf{D}^{\hat{\tau}_i}_{\mathrm{isi\ bs}\leftarrow\mathrm{pbs}}\mathbf{D}^{\hat{\tau}_i}_{ij}\left(\mathbf{D}^{\mathrm{sb},\hat{\tau}_j}_{\mathrm{pbs}\leftarrow\mathrm{pmc}}\nu^{\mathrm{m}}_{ji}\hat{\tau}^{\hat{\tau}_j}_{j}(\tau) + \nu^{\mathrm{m}}_{ji}M^{\hat{\tau}_j}_{ji}(\tau)\right)\\ &- \left(\mathbf{D}^{\mathrm{sb},\hat{\tau}_i}_{\mathrm{isi\ bs}\leftarrow\mathrm{pmc}}\nu^{\mathrm{m}}_{ij}\hat{\tau}^{\hat{\tau}_i}_{i}(\tau) + \nu^{\mathrm{m}}_{ij}M^{\hat{\tau}_i}_{ij}(\tau)\right)\Bigg\}.\end{aligned} \tag{23}$$

$\mathbf{D}^{\mathrm{sb}}_{\mathrm{pbs}\leftarrow\mathrm{pmc}}$ and $\mathbf{D}^{\mathrm{sb}}_{\mathrm{isi\ bs}\leftarrow\mathrm{pmc}}$ are the delay operators associated to the paths from the PMC to the PBS and from the PMC to the ISI BS, respectively. They can be decomposed into

$$\mathbf{D}^{\mathrm{sb}}_{(\mathrm{p\text{-}isi})\mathrm{bs}\leftarrow\mathrm{pmc}} = \mathbf{D}_{(\mathrm{p\text{-}isi})\mathrm{bs}\leftarrow\mathrm{eom}}\mathbf{D}_{\mathrm{eom}\leftarrow\mathrm{pmc}}\mathbf{D}_{\mathrm{up}}. \tag{24}$$

$\mathbf{D}_{\mathrm{up}}$ is the up-conversion delay due to phase-locking a 2.40(1) GHz oscillator to the 80 MHz PMC signal, and $\mathbf{D}_{\mathrm{eom}\leftarrow\mathrm{pmc}}$ is the cable delay from the PMC to the EOM. ν^{m}_{ij} is the up-converted USO frequency associated to MOSA_{ij}. Since Eq. (23) is expressed in the SCET, all clock imperfections are included into $\hat{\tau}^{\hat{\tau}_i}_i(\tau)$. The modulation noise $M^{\hat{\tau}_i}_{ij}$ contains any additional jitter collected on the path $\mathbf{D}^{\mathrm{sb}}_{(\mathrm{p\text{-}isi})\mathrm{bs}\leftarrow\mathrm{pmc}}$, e.g., due to the electrical frequency up-converters. The amplitude spectral densities (ASDs) of the modulation noise for left- and right-handed MOSAs are specified to be below [5,18]

$$\sqrt{S_{M_l}(f)} = 2.5\times10^{-6}\ \mathrm{m\,Hz^{-0.5}}\left(\frac{f}{\mathrm{Hz}}\right)^{-2/3}, \tag{25}$$

$$\sqrt{S_{M_r}(f)} = 2.5\times10^{-5}\ \mathrm{m\,Hz^{-0.5}}\left(\frac{f}{\mathrm{Hz}}\right)^{-2/3}. \tag{26}$$

The modulation noise on left-handed MOSAs is one order of magnitude lower, because the pilot tone for the ADC jitter correction (it is the ultimate phase reference) is derived from the 2.400 GHz clock signal.

To derive a pseudorange observation equation from the sideband beat note, we expand Eq. (23) using Eq. (2). We apply $\mathbf{A}^{\mathrm{sb}}_{\mathrm{pbs}\leftarrow\mathrm{dec}}$ to avoid nested delays in the pseudorange:

$$\begin{aligned}\mathbf{A}^{\mathrm{sb},\hat{\tau}_i}_{\mathrm{pbs}\leftarrow\mathrm{dec}}\left(\mathrm{ISI}^{\hat{\tau}_i}_{ij}(\tau) - \mathrm{ISI}^{\hat{\tau}_i}_{\mathrm{sb},ij}(\tau)\right) &= -\nu^{\mathrm{m}}_{ji}\mathbf{D}^{\hat{\tau}_i}_{ij}\left(\mathbf{D}^{\mathrm{sb},\hat{\tau}_j}_{\mathrm{pbs}\leftarrow\mathrm{pmc}}\hat{\tau}^{\hat{\tau}_j}_{j}(\tau) + M^{\hat{\tau}_j}_{ji}(\tau)\right) + \nu^{\mathrm{m}}_{ij}\mathbf{A}^{\hat{\tau}_i}_{\mathrm{pbs}\leftarrow\mathrm{isi\ bs}}\left(\mathbf{D}^{\mathrm{sb},\hat{\tau}_i}_{\mathrm{isi\ bs}\leftarrow\mathrm{pmc}}\hat{\tau}^{\hat{\tau}_i}_{i}(\tau) + M^{\hat{\tau}_i}_{ij}\right)\\ &= \left(\nu^{\mathrm{m}}_{ij} - \nu^{\mathrm{m}}_{ji}\right)\tau + \nu^{\mathrm{m}}_{ji}R^{\hat{\tau}_i}_{ij}(\tau) + \nu^{\mathrm{m}}_{ji}\cdot d^{\hat{\tau}_j}_{\mathrm{pbs}\leftarrow\mathrm{pmc}} - \nu^{\mathrm{m}}_{ij}\cdot\left(d^{\hat{\tau}_i}_{\mathrm{isi\ bs}\leftarrow\mathrm{pmc}} - d^{\hat{\tau}_i}_{\mathrm{pbs}\leftarrow\mathrm{isi\ bs}}\right)\\ &\quad + \nu^{\mathrm{m}}_{ij}\mathbf{A}^{\hat{\tau}_i}_{\mathrm{pbs}\leftarrow\mathrm{isi\ bs}}M^{\hat{\tau}_i}_{ij}(\tau) - \nu^{\mathrm{m}}_{ji}\mathbf{D}^{\hat{\tau}_i}_{ij}M^{\hat{\tau}_j}_{ji}(\tau).\end{aligned} \tag{27}$$

We subtract the 1 MHz ramp and then refer to Eq. (27) as SBR. Taking into account that the SBR phase is defined up to a cycle, the SBR can be written as

$$\begin{aligned}\mathrm{SBR}_{ij}^{\hat{\tau}_i}(\tau) &= \mathbf{A}_{\mathrm{pbs}\leftarrow\mathrm{dec}}^{\mathrm{sb},\hat{\tau}_i}\left(\mathrm{ISI}_{ij}^{\hat{\tau}_i}(\tau) - \mathrm{ISI}_{\mathrm{sb},ij}^{\hat{\tau}_i}(\tau)\right) \pm 1\ \mathrm{MHz}\tau \\ &= \nu_{ji}^{\mathrm{m}} R_{ij}^{\hat{\tau}_i}(\tau) + O_{ij}^{\mathrm{sb}} + N_{ij}^{\mathrm{sb}}(\tau) - a_{ij}^{\mathrm{sb}}(\tau). \end{aligned} \tag{28}$$

a_{ij}^{sb} denote the SBR ambiguity integers. Expressed as length, the SBR ambiguity is 12.5 cm, corresponding to the wavelength of the GHz sidebands. The SBR offset

$$O_{ij}^{\mathrm{sb}} = \nu_{ji}^{\mathrm{m}} \cdot d_{\mathrm{pbs}\leftarrow\mathrm{pmc}}^{\hat{\tau}_j} - \nu_{ij}^{\mathrm{m}} \cdot \left(d_{\mathrm{isi\ bs}\leftarrow\mathrm{pmc}}^{\hat{\tau}_i} - d_{\mathrm{pbs}\leftarrow\mathrm{isi\ bs}}^{\hat{\tau}_i}\right) \tag{29}$$

can be thought of as the differential phase accumulation of local and distant PMC signals on their paths to the respective PBSs. Similar to the PRNR offset, the SBR offset could be measured on ground. N_{ij}^{sb} denotes the appearance of the modulation noise in the SBR:

$$N_{ij}^{\mathrm{sb}} = \nu_{ij}^{\mathrm{m}} \mathbf{A}_{\mathrm{pbs}\leftarrow\mathrm{isi\ bs}}^{\hat{\tau}_i} M_{ij}^{\hat{\tau}_i}(\tau) - \nu_{ji}^{\mathrm{m}} \mathbf{D}_{ij}^{\hat{\tau}_i} M_{ji}^{\hat{\tau}_j}(\tau). \tag{30}$$

This is a combination of left- and right-handed modulation noise; their rms amplitudes are 2.9×10^{-5} m and 2.9×10^{-4} m, respectively. As shown in [5], it is possible to combine carrier and sideband beat notes from the RFI to form measurements of the dominating right-handed modulation noise, which can, thus, be subtracted from the SBRs (see Appendix B).

The advancement operator $\mathbf{A}_{\mathrm{pbs}\leftarrow\mathrm{dec}}^{\mathrm{sb}}$ [see Eq. (27)] is associated to the delay operator $\mathbf{D}_{\mathrm{dec}\leftarrow\mathrm{pbs}}^{\mathrm{sb}}$, to which we refer as sideband timestamping delay. The sideband timestamping delay can be decomposed into

$$\begin{aligned}\mathbf{D}_{\mathrm{dec}\leftarrow\mathrm{pbs}}^{\mathrm{sb}} = \mathbf{D}_{\mathrm{dec}}^{\mathrm{sb}} \mathbf{D}_{\mathrm{dpll}}^{\mathrm{sb}} \mathbf{D}_{\mathrm{dpll}\leftarrow\mathrm{abee}} \mathbf{D}_{\mathrm{abee}}^{\mathrm{sb}} \\ \mathbf{D}_{\mathrm{abee}\leftarrow\mathrm{qpr}} \mathbf{D}_{\mathrm{qpr}}^{\mathrm{sb}} \mathbf{D}_{\mathrm{qpr}\leftarrow\mathrm{pbs}}; \end{aligned} \tag{31}$$

these constituents are marked green in Fig. 4. As for the PRNR timestamping delay, we propose to individually calibrate all its constituents on ground. The sideband timestamping delay can then be compensated in an initial data treatment by application of its associated advancement operator [see Eq. (27)].

In reality, the beat notes are expected to be delivered not in phase but in frequency with occasional phase anchor points. Therefore, we consider the derivative of Eq. (28); we refer to it as sideband range rate (SB$\dot{\mathrm{R}}$):

$$\dot{\mathrm{SBR}}_{ij}^{\hat{\tau}_i}(\tau) = \nu_{ji}^{\mathrm{m}} \dot{R}_{ij}^{\hat{\tau}_i}(\tau) + \dot{N}_{ij}^{\mathrm{sb}}(\tau). \tag{32}$$

The sideband range rates are an offset-free and unambiguous measurement of the pseudorange time derivatives. Phase anchor points enable their integration, so that we recover Eq. (28).

C. Time-delay interferometric ranging (TDIR)

TDI builds combinations of delayed ISI and RFI carrier beat notes to virtually form equal-arm interferometers, in which laser frequency noise is suppressed. In the alternative TDI topology, the corresponding TDI delays $\mathcal{D}_{ij}$ are given by the pseudoranges in combination with onboard delays [see Eq. (13)]. TDIR turns the main scientific data streams themselves into an absolute ranging observable: It minimizes the power integral of the laser frequency noise in the TDI combinations by varying the delays that are applied to the beat notes [12]. When doing this before clock synchronization to TCB, i.e., with the beat notes sampled according to the respective SCETs, the TDI delays $\mathcal{D}_{ij}$ show up at the very minimum of that integral. Thus, TDIR constitutes an unbiased observable of the TDI delays $\mathcal{D}_{ij}$, which requires only the interferometric measurements.

Below, we consider TDI in frequency [14]. Therefore, we introduce the Doppler-delay operator associated to the TDI delay:

$$\dot{\mathcal{D}}_{ij}^{\hat{\tau}_i} f^{\hat{\tau}_j}(\tau) = \left(1 - \dot{R}_{ij}^{\hat{\tau}_i}(\tau)\right) \mathcal{D}_{ij}^{\hat{\tau}_i} f^{\hat{\tau}_j}(\tau). \tag{33}$$

Here, we assume the onboard delay constituents of $\mathcal{D}_{ij}^{\hat{\tau}_i}$ to be slowly time varying, so that only the pseudorange time derivative appears in the Doppler factor. We use the shorthand notation

$$\dot{\mathcal{D}}_{ijk}^{\hat{\tau}_i} = \dot{\mathcal{D}}_{ij}^{\hat{\tau}_i} \dot{\mathcal{D}}_{jk}^{\hat{\tau}_j} \tag{34}$$

to indicate chained Doppler-delay operators. In this paper, we neglect onboard delays in the RFI beat notes. We start our consideration of TDIR from the intermediary TDI variables η_{ij}. These are combinations of the ISI and RFI carrier beat notes to eliminate the laser frequency noise contributions of right-handed lasers. In terms of the η_{ij}, the second-generation TDI Michelson variables can be expressed as [19]

$$\begin{aligned} X_2^{\hat{\tau}_1} = &\left(1 - \dot{\mathcal{D}}_{121}^{\hat{\tau}_1} - \dot{\mathcal{D}}_{12131}^{\hat{\tau}_1} + \dot{\mathcal{D}}_{1312121}^{\hat{\tau}_1}\right)\left(\eta_{13}^{\hat{\tau}_1} - \dot{\mathcal{D}}_{13}^{\hat{\tau}_1}\eta_{31}^{\hat{\tau}_3}\right) \\ &- \left(1 - \dot{\mathcal{D}}_{131}^{\hat{\tau}_1} - \dot{\mathcal{D}}_{13121}^{\hat{\tau}_1} + \dot{\mathcal{D}}_{1213131}^{\hat{\tau}_1}\right)\left(\eta_{12}^{\hat{\tau}_1} - \dot{\mathcal{D}}_{12}^{\hat{\tau}_1}\eta_{21}^{\hat{\tau}_2}\right). \end{aligned} \tag{35}$$

$Y_2^{\hat{\tau}_2}$ and $Z_2^{\hat{\tau}_3}$ are obtained by cyclic permutation of the indices. For later reference, we also state the first-generation TDI Michelson variables:

$$X_1^{\hat{\tau}_1} = (1 - \dot{\mathcal{D}}_{121}^{\hat{\tau}_1})\left(\eta_{13}^{\hat{\tau}_1} - \dot{\mathcal{D}}_{13}^{\hat{\tau}_1}\eta_{31}^{\hat{\tau}_3}\right) - (1 - \dot{\mathcal{D}}_{131}^{\hat{\tau}_1})\left(\eta_{12}^{\hat{\tau}_1} - \dot{\mathcal{D}}_{12}^{\hat{\tau}_1}\eta_{21}^{\hat{\tau}_2}\right). \tag{36}$$

In the framework of TDIR, the delays applied in TDI are parametrized by a model, e.g., by a polynomial model. We minimize the power integral of the TDI combinations by varying the model parameters. TDIR attempts to minimize the in-band laser frequency noise residual. Therefore, we apply a bandpass filter to first remove other contributions appearing out of band, i.e., slow drifts and contributions above 1 Hz that are dominated by aliasing and interpolation errors. We use the TDIR estimator

$$\mathrm{TDIR}_{ij}^{\hat{\tau}_i} = \min_{\Theta} \frac{1}{T}\int_{\frac{1}{T}}^{T} \left[\tilde{X}_2^{\hat{\tau}_1}\right]^2 + \left[\tilde{Y}_2^{\hat{\tau}_2}\right]^2 + \left[\tilde{Z}_2^{\hat{\tau}_3}\right]^2 \mathrm{d}t, \tag{37}$$

similar to the one proposed by [12].[3] Θ denotes the parameters of the delay model, and the tilde indicates the filtered TDI combinations.

The TDIR accuracy, denoted by σ^{tdir}, increases with the integration time T (length of telemetry dataset). It is on the order of [12]

$$\sigma^{\mathrm{tdir}}(T) \propto 10\ \mathrm{cm}\sqrt{\frac{\mathrm{d}}{T}}, \tag{38}$$

where d stands for day. Hence, we require about 1000s of data to reach meter accuracy.

D. Ground-observation-based ranging (GOR)

The mission operation center (MOC) provides orbit determinations (ODs) via the ESA tracking stations and MOC time correlations (MOC TCs). When combined properly, these two on-ground measurements form a pseudorange observable referred to as ground-observation-based ranging (GOR). It has an uncertainty of about 50 km due to uncertainties in both the OD and the MOC TC. Yet, it yields valuable information. It is unambiguous; hence, it can be used to resolve the PRNR ambiguities.

The OD yields information about the absolute positions and velocities of the three SC. New orbit determinations are published every few days. For the position and velocity measurements in the line of sight, radial (with respect to the Sun) and cross-track direction conservative estimations by ESA state the uncertainties as 2 km and 4 mm s^{-1}, 10 km and 4 mm s^{-1}, and 50 km and 5 cm s^{-1}, respectively [20]. The MOC TC is a measurement of the SCET desynchronization from TCB. It is determined during the telemetry contacts via a comparison of the SCET associated to the emission of a telemetry packet and the TCB of its reception on Earth taking into account the down link delay. We expect the accuracy of the MOC TC to be better than 0.1 ms (corresponds to 30 km). This uncertainty is due to inexact knowledge of the SC-to-ground-station separation, as well as inaccuracies in the time tagging process on board and on ground.

As shown in Appendix A, the pseudorange can be expressed in TCB as a function of the reception time:

$$R_{ij}^t(t) = (1 + \delta\dot{\hat{\tau}}_j^t(t)) \cdot d_{ij}^t(t) + \delta\hat{\tau}_{ij}^t(t). \tag{39}$$

d_{ij}^t denotes the light travel time from SC j to SC i, $\delta\hat{\tau}_{ij}^t$ the offset between the involved SCETs, and $\delta\dot{\hat{\tau}}_j^t$ the SCET drift of the emitting SC with respect to TCB. The light travel times can be expressed in terms of the ODs [21]:

$$d_{\mathrm{od},ij}^t(t) = \frac{1}{c}L_{ij}^t(t) + \frac{1}{c^2}\vec{L}_{ij}^t(t)\cdot\vec{v}_j^t(t) + O(c^{-3}), \tag{40}$$

$$\vec{L}_{ij} = \vec{r}_i - \vec{r}_j, \qquad L_{ij} = |\vec{L}_{ij}|. \tag{41}$$

$\vec{r}_i$ denotes the position of the receiving SC, and $\vec{r}_j$ and $\vec{v}_j$ are position and velocity, respectively, of the emitting one. The $O(c^{-3})$ terms contribute to the light travel time at the order of 10 m. They are negligible compared to the large uncertainties of the orbit determination. Combining these light travel time estimates with the MOC TCs allows us to write the GOR as

$$\mathrm{GOR}_{ij}^t(t) = d_{\mathrm{od},ij}^t(t) + \delta\hat{\tau}_{\mathrm{tc},ij}^t(t) = R_{ij}^t(t) + N_{ij}^{\mathrm{gor}}, \tag{42}$$

$$\delta\hat{\tau}_{\mathrm{tc},ij}^t(t) = \delta\hat{\tau}_{\mathrm{tc},i}^t(t) - \delta\hat{\tau}_{\mathrm{tc},j}^t(t). \tag{43}$$

$\delta\hat{\tau}_{\mathrm{tc},i}^t$ denotes the MOC TC of SC i and $N^{\mathrm{gor}} \sim 50$ km the GOR uncertainty. Note that the ODs and the MOC TCs (hence, also the GOR) are given in TCB, while all other pseudorange observables are sampled in the respective SCETs. This desynchronization is negligible: The desynchronization can amount up to 10 s after the ten-year mission time, and the pseudoranges drift with 10 to 100 m s^{-1} (see central plot in Fig. 6). Hence, neglecting the desynchronization leads to errors of about 100 to 1000 m, which are negligible compared to the large GOR uncertainty.

[3]Note that this is not the optimal TDIR estimator, as the noise shapes and the correlations between different channels are not taken into account.

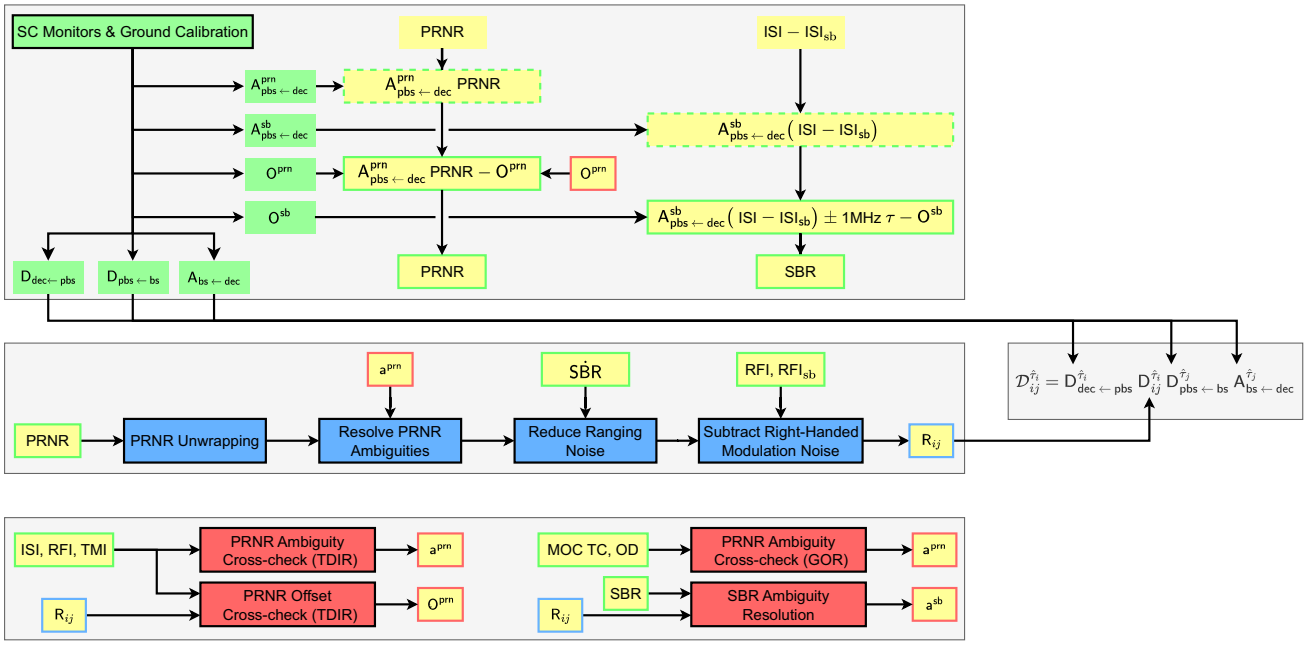

FIG. 5. We illustrate the three-stage ranging sensor fusion. Processing elements are drawn with a black frame. In the upper part, we show the initial data treatment. Products of the on-ground calibration (the various delays and offsets) are drawn green. Raw datasets are drawn yellow; after the initial data treatment, we add a green frame. In the central part, we show the core ranging processing. Its output, the pseudoranges, are drawn with a blue frame. In the right box, we show how the pseudoranges are combined with onboard delays to form the TDI delays. In the lower part, we show simultaneous cross-checks of PRNR ambiguity, PRNR offset, and SBR ambiguity. Products of these cross-checks are drawn with a red frame.

IV. RANGING SENSOR FUSION

To combine the four pseudorange observables, we propose a three-stage ranging sensor fusion (RSF) consisting of an initial data treatment, a ranging processing, and cross-checks. The ranging processing (central part in Fig. 5) refers to the ranging-related routines, which need to run continuously during operation. These are the PRNR unwrapping and the reduction of ranging and right-handed modulation noise. Simultaneously, the PRNR ambiguities and offsets are continuously cross-checked using TDIR and GOR (lower part in Fig. 5). Both ranging processing and cross-checks rely on a preceding initial data treatment (upper part in Fig. 5), in which the various delays and offsets are compensated for. Ranging processing and cross-checks can be categorized into four parts demonstrated below: PRNR ambiguity, noise reduction, PRNR offset, and SBR ambiguity.

The RSF delivers accurate and precise pseudorange estimates. To put the RSF into the context of LISA data processing, we revisit Fig. 1: In the baseline TDI topology, the pseudorange estimates from the RSF are disentangled into light travel times and differential timer offsets [see Eq. (A5)]. The differential timer offsets are used to synchronize the interferometric measurements, and the light travel times serve as delays in TDI. In the alternative topology, TDI is executed on the unsynchronized beat notes. Here, the pseudorange estimates from the RSF are directly used as delays in TDI, after they have been combined with onboard delays according to Eq. (13).

A. PRNR ambiguity

As part of the ranging processing, the PRNR needs to be steadily unwrapped: Because of the finite PRN code length, the PRNR jumps back to 0 km when crossing 400 km and vice versa (see upper plot in Fig. 6). These jumps are unphysical but easy to identify and to remove. Apart from that, the PRNR ambiguities need to be cross-checked regularly. For that purpose, we propose two independent methods below.

GOR represents an unambiguous pseudorange observable. Hence, the combination of PRNR and GOR enables an identification of the PRNR ambiguity integers a_{ij}^{prn}:

$$\mathrm{GOR}_{ij}^{t}(t)-\mathrm{PRNR}_{ij}^{\hat{\tau}_i}(\tau)=N_{ij}^{\mathrm{gor}}+a_{ij}^{\mathrm{prn}}(\tau)\cdot 400\,\mathrm{km}+\underbrace{R_{ij}^{t}(t)-R_{ij}^{\hat{\tau}_i}(\tau)-O_{ij}^{\mathrm{prn}}-N_{ij}^{\mathrm{prn}}(\tau)}_{\text{negligible}}, \tag{44}$$

$$a_{ij}^{\mathrm{prn}}(\tau)=\mathrm{round}\left[\frac{\mathrm{GOR}_{ij}^{t}(t)-\mathrm{PRNR}_{ij}^{\hat{\tau}_i}(\tau)}{400\ \mathrm{km}}\right], \tag{45}$$

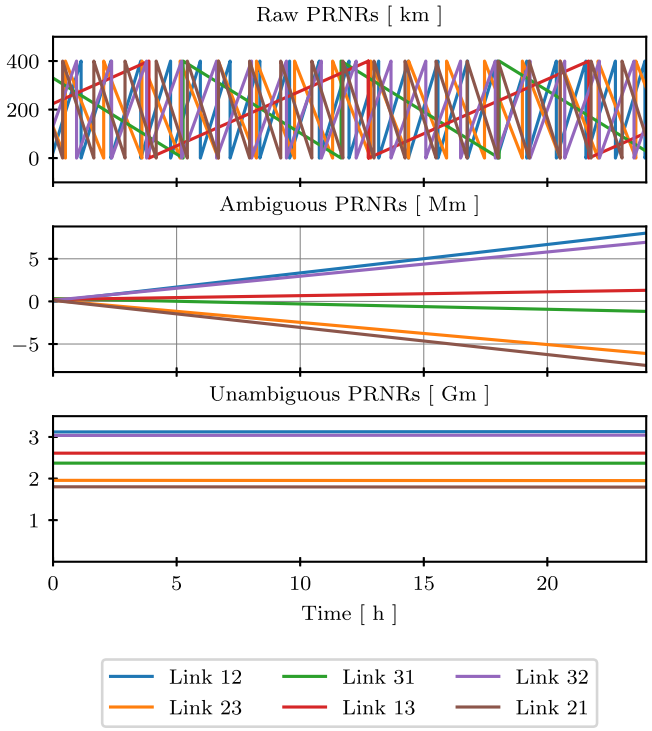

FIG. 6. Upper plot: raw PRNR. The ambiguity jumps at 0 km and 400 km can be seen. Central plot: ambiguous PRNR, the jumps have been removed but the PRNR ambiguities have not been resolved yet. The large slopes are mainly due to USO frequency offsets. Lower plot: unambiguous PRNR. The large differences between the links are caused by differential SCET offsets.

where 400 km is the value we assumed for the PRN code length. However, this procedure succeeds only if $|N_{ij}^{\mathrm{gor}}|$ does not exceed the PRN code's half length, i.e., 200 km. Otherwise, a wrong value for the associated PRN ambiguity integer is selected, resulting in an estimation error of 400 km in the corresponding link. Note that $\mathrm{GOR}_{ij}^{t}(t)$ and $\mathrm{PRNR}_{ij}^{\hat{\tau}_i}(\tau)$ are sampled according to different time frames, but this desynchronization is negligible considering the low accuracy required here (see Sec. III D).

TDIR constitutes an unambiguous pseudorange observable, too. Hence, it can be applied as an independent cross-check of the PRNR ambiguities. We linearly detrend the ISI, RFI, and TMI beat notes. We then form the first-generation TDI Michelson variables [see Eq. (36)] assuming a constant model for the delays. The pseudoranges are actually drifting by 10 to 100 $\mathrm{m\,s^{-1}}$ mainly due to differential USO frequency offsets (see central plot in Fig. 6). Therefore, we choose a short integration time (we use 150 s); otherwise, the constant delay model is not sufficient. We use the GOR estimates from above as initial delay values in the TDIR estimator. The TDIR estimator then estimates the six pseudoranges as constants, which can be used to resolve the PRNR ambiguity integers:

$$a_{ij}^{\mathrm{prn}}(\tau) = \mathrm{round}\left[\frac{\mathrm{TDIR}_{ij}^{\hat{\tau}_i}(\tau) - \mathrm{PRNR}_{ij}^{\hat{\tau}_i}(\tau)}{400\ \mathrm{km}}\right]. \tag{46}$$

It is not necessary to apply second-generation TDI; the first-generation already accomplishes the task (see Fig. 9).

B. Noise reduction

For the ranging noise reduction in the ranging processing, we propose to combine PRNR and sideband range rates in a modified version of a linearized Kalman filter (KF). The conventional KF requires all measurements to be sampled according to one universal time grid. However, in LISA each SC involves its own SCET. We circumvent this difficulty by splitting up the system and build one KF per SC. Each KF processes only the measurements taken on its associated SC, so that the individual SCETs serve as time grids.

The state vector of the KF belonging to SC 1 and its associated linear system model can be expressed as

$$x^{\hat{\tau}_1} = (R_{12}^{\hat{\tau}_1}, R_{13}^{\hat{\tau}_1}, \dot{R}_{12}^{\hat{\tau}_1}, \dot{R}_{13}^{\hat{\tau}_1}, \ddot{R}_{12}^{\hat{\tau}_1}, \ddot{R}_{13}^{\hat{\tau}_1})^{\intercal}, \tag{47}$$

$$x_{k+1}^{\hat{\tau}_1} = \begin{pmatrix} 1 & 0 & \Delta t & 0 & \frac{\Delta t^2}{2} & 0 \\ 0 & 1 & 0 & \Delta t & 0 & \frac{\Delta t^2}{2} \\ 0 & 0 & 1 & 0 & \Delta t & 0 \\ 0 & 0 & 0 & 1 & 0 & \Delta t \\ 0 & 0 & 0 & 0 & 1 & 0 \\ 0 & 0 & 0 & 0 & 0 & 1 \end{pmatrix} \cdot x_k^{\hat{\tau}_1} + w_k^{\hat{\tau}_1}, \tag{48}$$

k being a discrete time index. Equation (48) describes the time evolution of the state vector from k to $k+1$. $w_k^{\hat{\tau}_1}$ denotes the process noise vector. In our implementation, its covariance matrix W is set

$$\mathrm{E}[w_k \cdot w_l^{\mathrm{T}}] = \delta_{k,l} W, \tag{49}$$

$$W = \mathrm{diag}(0, 0, 0, 0, 10^{-15}\ \mathrm{s^{-1}}, 10^{-15}\ \mathrm{s^{-1}})^2, \tag{50}$$

and $\delta_{k,l}$ denotes the Kronecker delta. The measurement vector and the associated observation model are given by

$$y^{\hat{\tau}_1} = (\mathrm{PRNR}_{12}^{\hat{\tau}_1}, \mathrm{PRNR}_{13}^{\hat{\tau}_1}, \mathrm{S\dot{B}R}_{12}^{\hat{\tau}_1}, \mathrm{S\dot{B}R}_{13}^{\hat{\tau}_1})^{\intercal}, \tag{51}$$

$$y_k^{\hat{\tau}_1} = \begin{pmatrix} 1 & 0 & 0 & 0 & 0 & 0 \\ 0 & 1 & 0 & 0 & 0 & 0 \\ 0 & 0 & 2.401\ \mathrm{GHz} & 0 & 0 & 0 \\ 0 & 0 & 0 & 2.400\ \mathrm{GHz} & 0 & 0 \end{pmatrix} \cdot x_k^{\hat{\tau}_1} + v_k^{\hat{\tau}_1}. \tag{52}$$

Equation (52) relates the measurement vector to the state vector. $v_k^{\hat{\tau}_1}$ denotes the measurement noise vector. In our implementation, its covariance matrix V is set

$$\mathrm{E}[v_k \cdot v_l^{\mathrm{T}}] = \delta_{k,l} V, \tag{53}$$

$$V = \mathrm{diag}\Big(3\times10^{-9}\ \mathrm{s}, 3\times10^{-9}\ \mathrm{s}, 5.2\times10^{-13}, 5.2\times10^{-13}\Big)^2. \tag{54}$$

The diagonal entries denote the variances of the respective measurements. We assume the measurements to be uncorrelated, so that the off-diagonal terms are zero. The KFs for SC 2 and SC 3 are defined accordingly. Hence, we remove the ranging noise and obtain estimates for all the six pseudoranges and their time derivatives.

These pseudorange estimates are dominated by the right-handed modulation noise, which is one order of magnitude higher than the left-handed one. As pointed out in [5], the right-handed modulation noise can be subtracted (see Appendix B): We combine the RFI measurements to form the ΔM_i, which are measurements of the right-handed modulation noise on SC i [see Eq. (B4)]. For right-handed MOSAs, the local right-handed modulation noise enters the sideband range rates, and we just need to subtract the local ΔM_i [see Eq. (B5b)]. For left-handed MOSAs, the Doppler-delayed right-handed modulation noise from the distant SC appears in the sideband range rates. Here, we need to apply the Kalman filter estimates for the pseudoranges and their time derivatives to form the Doppler-delayed distant ΔM_i, which then can be subtracted [see Eq. (B5a)]. We then process the three KFs again, this time with the corrected sideband range rates. Now they are limited by left-handed modulation noise, so that the respective noise levels are lower. Therefore, we need to adjust the measurement noise covariance matrix for the second run of the KFs:

$$V_{\mathrm{cor}} = \mathrm{diag}\Big(3\times10^{-9}\ \mathrm{s}, 3\times10^{-9}\ \mathrm{s}, 7.4\times10^{-14}, 7.4\times10^{-14}\Big)^2. \tag{55}$$

In this way, we obtain estimates for the pseudoranges and their time derivatives, which are limited by the left-handed modulation noise.

C. PRNR offset

The PRNR offset is calibrated on ground before mission start. During operation, it is constructed with the help of SC monitors and subtracted in the initial data treatment.

TDIR can be used as a cross-check for residual PRNR offsets, as it is sensitive to offsets in the delays. To obtain optimal performance, we choose the second-generation TDI Michelson variables [see Eq. (35)] to be ultimately limited by secondary noises. In-band clock noise is sufficiently suppressed, since we operate on beat notes in total frequency and make use of the in-band ranging information provided by the preceding noise reduction step. Accordingly, the offset delay model is parametrized by

$$d_{ij}^{\hat{\tau}_i}(\tau) = \hat{R}_{ij}^{\hat{\tau}_i}(\tau) - O_{ij}, \tag{56}$$

where $\hat{R}_{ij}^{\hat{\tau}_i}$ denote the pseudorange estimates after noise reduction and O_{ij} are the six offset parameters. As discussed in Sec. III C, computing TDI in total frequency units generally results in a variable with residual trends. Those trends need to be removed prior to calculation of the TDIR integral to be sensitive to residual laser noise in band. This is achieved by an appropriate bandpass filter with a passband from 0.1 to 1 Hz. The TDIR integral then reads

$$\hat{O}_{ij} = \arg\min_{O_{ij}} \int_0^T \tilde{X}^2(t) + \tilde{Y}^2(t) + \tilde{Z}^2(t)\mathrm{d}t, \tag{57}$$

where tilde indicates the filtered quantities. $\hat{O}_{ij}$ are the estimated offset parameters.

D. SBR ambiguity

Phase anchor points in combination with the pseudorange estimates after noise reduction enable the SBR ambiguity resolution [see Eq. (28)]:

$$a_{ij}^{\mathrm{sb}}(\tau) = \mathrm{round}\left[\nu_{ji}^{\mathrm{m}} \hat{R}_{ij}^{\hat{\tau}_i}(\tau) - \mathrm{SBR}_{ij}^{\hat{\tau}_i}(\tau)\right], \tag{58}$$

where $\mathrm{SBR}_{ij}^{\hat{\tau}_i}$ are the phase anchor points and $\hat{R}_{ij}^{\hat{\tau}_i}$ the pseudorange estimates of the core ranging processing pipeline. Thus, we obtain estimates of the SBR ambiguity integers a_{ij}^{sb}. These can be used to compute unambiguous SBR pseudorange estimates associated to the phase anchor points, which serve as initial values for the integration of the sideband range rates [Eq. (32)]. This procedure is successful if the $\hat{R}_{ij}^{\hat{\tau}_i}$ are more accurate than 6.25 cm (half the SBR ambiguity). Then, SBR constitutes a very accurate pseudorange observable, as not only its precision but also its accuracy are limited by the modulation noise, in contrast to the $\hat{R}_{ij}^{\hat{\tau}_i}$, whose accuracy is ultimately limited by the ranging noise. We assume here that the SBR offset [Eq. (29)] is corrected in the initial data treatment.

V. RESULTS

In this section, we demonstrate the performance of our implementation of the core ranging processing and the cross-checks as proposed in Sec. IV (central and lower part in Fig. 5). We did not implement the initial data treatment. Instead, we assume that the PRNR and sideband time-stamping delays are compensated beforehand. We further

consider offset-free PRNR and apply TDIR as a cross-check for residual offsets.

We use telemetry data simulated by LISA Instrument [22] and LISANode [23] based on orbits provided by ESA [20,24]. We simulate phase anchor points for the SBR [see Eq. (28)]. The SCET deviations from the respective proper times are modeled as

$$\delta\hat{\tau}_i(\tau) = \delta\hat{\tau}_{i,0} + y_i\tau + \frac{\dot{y}_i}{2}\tau^2 + \frac{\ddot{y}_i}{3}\tau^3 + \int_{\tau_0}^{\tau} \mathrm{d}\tilde{\tau} y_i^{\epsilon}(\tilde{\tau}), \tag{59}$$

where the $\delta\hat{\tau}_{i,0}$ denote the initial SCET deviations set to 1, −1.2, and 0.6 s for SC 1, 2, and 3, respectively. The y_i model the PMC frequency offsets corresponding to linear clock drifts. They are set to 10^{-7}, -2×10^{-7}, and 0.6×10^{-7} for SC 1, 2, and 3, respectively. $\dot{y}_i \sim 10^{-14}$ s^{-1} and $\ddot{y}_i \sim 10^{-23}$ s^{-2} are constants modeling the linear and quadratic PMC frequency drifts. The y_i^{ϵ} denote the stochastic clock noise in fractional frequency deviations; the associated ASD is given by

$$\sqrt{S_{y^{\epsilon}}(f)} = 6.32\times10^{-14}\ \mathrm{Hz}^{-0.5}\left(\frac{f}{\mathrm{Hz}}\right)^{-0.5}. \tag{60}$$

We simulate laser frequency noise with an ASD of

$$\sqrt{S_{N^p}(f)} = 30\ \mathrm{Hz}^{-0.5} \tag{61}$$

and ranging and modulation noise as specified in Secs. III A and III B. Furthermore, we consider test-mass acceleration noise

$$\sqrt{S_{N^{\delta}}(f)} = 4.8\times10^{-15}\ \mathrm{m\,s^{-2}\,Hz^{-0.5}}\sqrt{1+\left(\frac{0.4\ \mathrm{mHz}}{f}\right)^2} \tag{62}$$

and readout noise

$$\sqrt{S_{N^{\mathrm{ro}}}(f)} = A\sqrt{1+\left(\frac{2\ \mathrm{mHz}}{f}\right)^4}, \tag{63}$$

where $A = 6.35\times10^{-12}$ mHz$^{-0.5}$ for the ISI carrier and $A = 1.25\times10^{-11}$ mHz$^{-0.5}$ for the ISI sideband beat notes. For the readout noise, we set a saturation frequency of $f_{\mathrm{sat}} = 0.1$ mHz, below which we whiten. The orbit determinations are simulated by LISA ground tracking with the noise levels specified in Sec. III D.

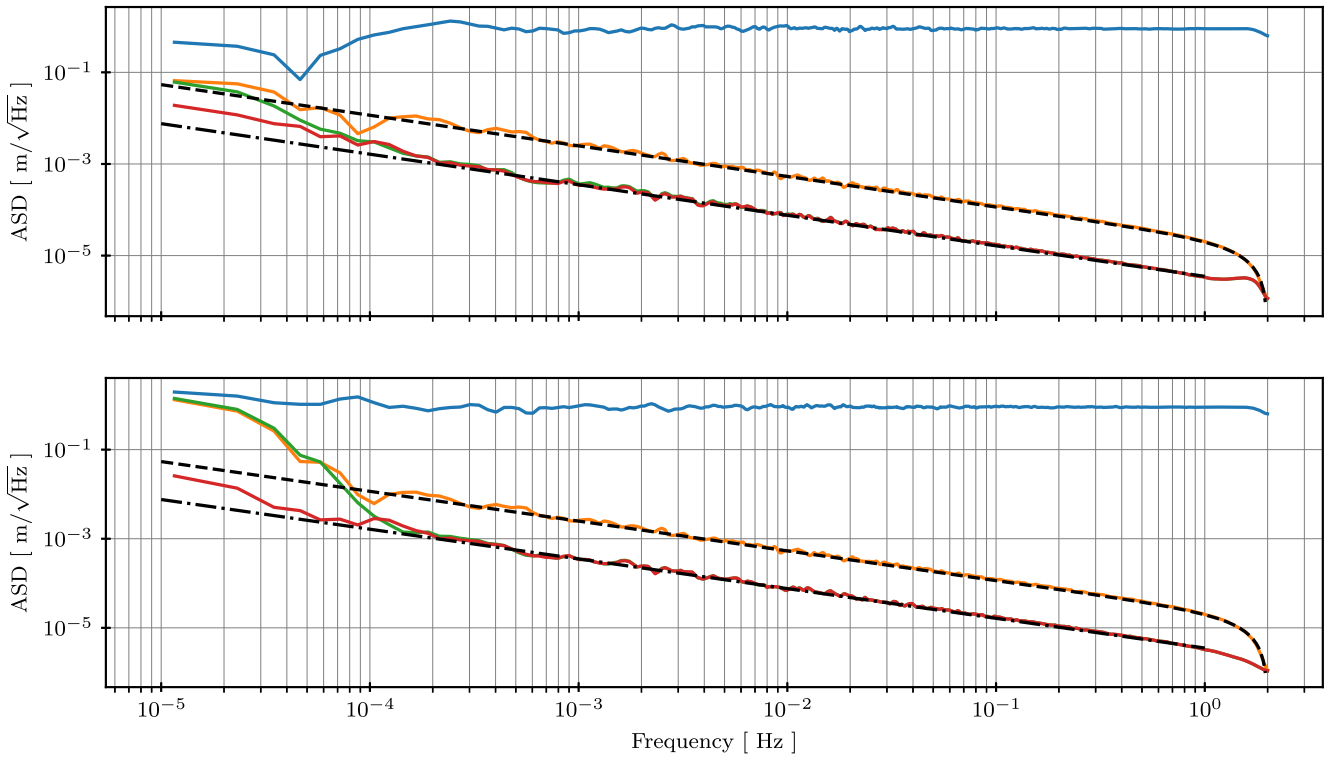

FIG. 7. ASDs of the residual pseudorange estimates for link 12 (upper plot) and link 21 (lower plot). In blue, residual PRNR. In orange, residual pseudorange estimates after ranging noise reduction. In green, residual pseudorange estimates after subtraction of right-handed modulation noise. In red, residual SBR. Dashed black lines: right-handed modulation noise model. Dash-dotted black lines: left-handed modulation noise model.

A. Ranging processing

Here, we demonstrate the performance of our implementation of the core ranging processing for one day of telemetry data simulated by LISA Instrument [22]. The first ranging processing step covers the PRNR unwrapping (see Fig. 6). The upper plot shows the raw PRNR, which jumps back to 0 km when crossing 400 km and vice versa. These jumps are easy to identify and to remove. In our implementation, we remove all PRNR jumps bigger than 200 km. The central plot shows the unwrapped but ambiguous PRNR. Here, we see PRNR drifts of the order of 10 to 100 $\mathrm{m\,s^{-1}}$, which are mainly due to differential USO frequency offsets. Inserting the PRNR ambiguity integers obtained from GOR and TDIR yields the unambiguous PRNR shown in the lower plot.

In the second step, we use the Kalman filter presented in Sec. IV to reduce the ranging noise. Subsequently, we subtract the right-handed modulation noise applying the ΔM measurements constructed from the RFI beat notes (see Appendix B). After noise reduction, we resolve the SBR ambiguities combining the estimated pseudoranges with the simulated SBR phase anchor points [see Eq. (58)]. We then integrate the sideband range rates, to obtain unambiguous SBR.

In Fig. 7, we plot the ASDs of the residual pseudorange estimates (deviations of the estimates from the true pseudorange values in the simulation) for link 12 (upper plot) and link 21 (lower plot). Blue lines show the ASDs of the residual PRNR, which are essentially the ASDs of the white ranging noises. The residual pseudorange estimates after ranging noise reduction are plotted in orange. They are obtained by combining the PRNR with the sideband range rates. Therefore, they are limited by right-handed modulation noise (dashed black line). In green, we plot the residual pseudorange estimates after subtraction of right-handed modulation noise with the RFI beat notes. Now the estimates are limited by left-handed modulation noise (dash-dotted black line). The residual SBR are drawn red; they are limited by left-handed modulation noise as well but involve a smaller offset, since the SBR phase anchor points are more accurate than PRNR after ranging noise reduction (see Fig. 8). In the case of left-handed MOSAs (see link 12), the RFI beat notes need to be time shifted to form the delayed ΔM measurements. We apply the time shifting method of PyTDI [25], which consists in a Lagrange interpolation (we use order 5). The interpolation introduces noise in the high-frequency band (see the bump at 2 Hz in the upper plot), but this is out of band.

Figure 8 shows the different residual pseudorange estimates as time series. The upper plot shows the six residual pseudorange estimates after ranging noise reduction, the second plot after subtraction of right-handed modulation noise. The third plot shows the SBR residuals. The subtraction of right-handed modulation noise reduces the noise floor, but it does not increase the accuracy of the pseudorange estimates. The accuracy can be increased by one order of magnitude through the resolution of the SBR ambiguities. After ambiguity resolution, SBR constitutes pseudorange estimates with submillimeter accuracy.

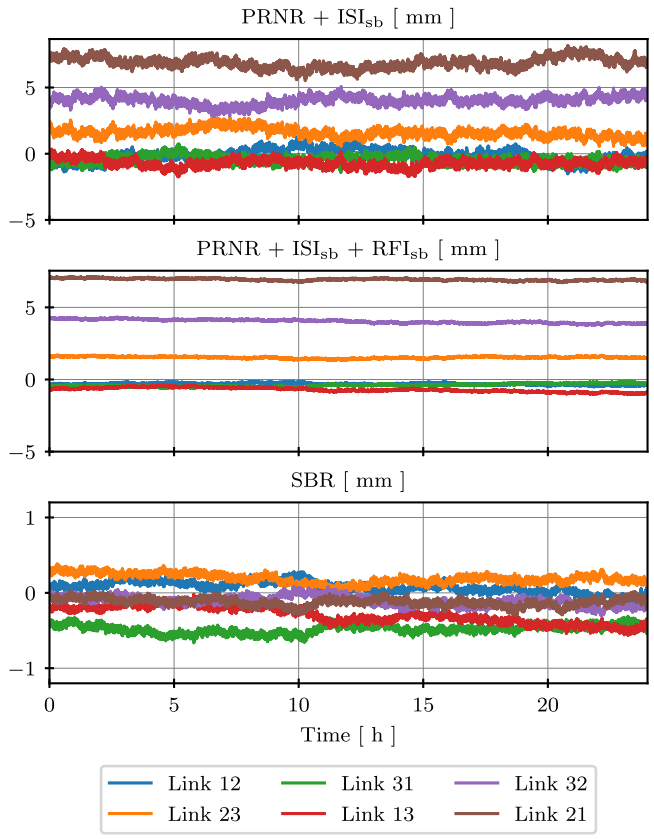

FIG. 8. Upper plot: residual pseudorange estimates after ranging noise reduction. Second plot: residual pseudorange estimates after subtraction of right-handed modulation noise. Third plot: residual SBR estimates.

B. Cross-checks

Here, we demonstrate the performance of our implementation of the cross-checks for PRNR ambiguity and PRNR offset.

The PRNR ambiguities can be resolved using either GOR [see Eq. (45)] or TDIR [see Eq. (46)]. To evaluate the performance of both methods, we simulate 1000 short (150 s) telemetry datasets with LISA Instrument [22] and one set of ODs and MOC TCs for each of them. We compute the GOR and TDIR pseudorange estimates for each of the 1000 datasets. Figure 9 shows the GOR residuals (first row) and the TDIR residuals (second row) in kilometers as histogram plots. We see that the GOR accuracy depends on the arm, because we obtain more accurate ODs for arms oriented in the line of sight direction than for those oriented cross-track. The PRNR ambiguity resolution via GOR is successful for GOR deviations smaller than 200 km. In the case of the links 23, 31, 13, and 32, all PRNR

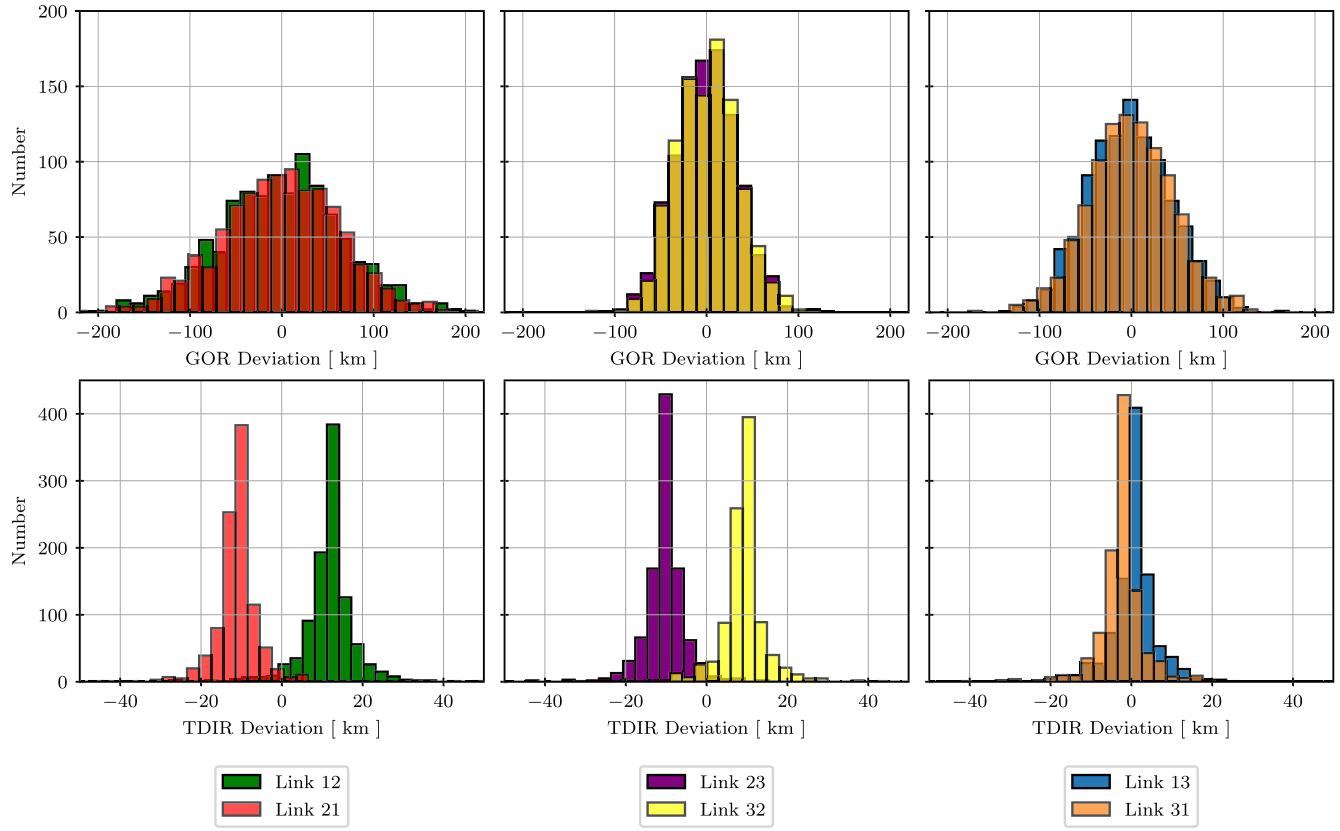

FIG. 9. PRNR ambiguity resolution via GOR (upper plots) and TDIR (lower plots). The histogram plots show the residual GOR and TDIR pseudorange estimates (deviations from true pseudorange) for the different links.

ambiguity resolutions via GOR are successful. For each of the links 12 and 21, two out of the 1000 PRNR ambiguity resolutions fail. The GOR estimates are passed as initial values to TDIR, which then reduces the uncertainty by almost one order of magnitude (lower plot in Fig. 9), such that eventually all PRNR ambiguity resolutions are successful. The direction-dependent offsets we observe in the TDIR estimates are due to the fact that we apply constant delays in the model used in the minimization of Eq. (57). In reality, these delays drift with time mainly due to the differential USO frequency offsets, and these drifts are opposite for counterpropagating links (central plot in Fig. 6). The offsets are not a problem, since the corresponding estimates are one order of magnitude more accurate than what we need.

TDIR can also be applied to estimate the PRNR offsets. Hence, it constitutes a cross-check of the on-ground PRNR offset calibration. We simulate one year of telemetry data using LISANode [23]. We set the PRNR offsets to 160.3, −210.2, 137.3, −250.3, −188.8, and 105.1 m for the links 12, 23, 31, 13, 32, and 21, respectively. We divide the dataset into 1-day chunks (left plots in Fig. 10), 2-day chunks (central plots in Fig. 10), and 3-day chunks (right plots in Fig. 10). In each partition, we apply the TDIR estimator presented in Sec. IV C to each chunk in order to estimate the PRNR offsets. This computation was parallelized and executed on the ATLAS cluster at the AEI Hannover. In the upper part in Fig. 10, we show the offset estimation residuals for the three chunk sizes. The offset estimation accuracy increases with the chunk size in agreement with the order of magnitude estimate through Eq. (38). In the lower part in Fig. 10, we plot the residual cumulative averages of the PRNR offset estimates for the different chunk sizes. Here, it can be seen that the TDIR estimator performs similarly for the different chunk sizes. With the 3-day chunk size, we can estimate all PRNR offsets with an accuracy of better than 20 cm after 10 days. The dashed black lines indicate 6.25 cm (half the SBR ambiguity). This is the required PRNR offset estimation accuracy for a successful SBR ambiguity resolution. All offset estimation residuals are below these 6.25 cm after 179 days.

VI. CONCLUSION

The onboard ranging system PRNR requires three treatments due to its ambiguity, offset, and noise. In this article, we propose a ranging sensor fusion (RSF), which uses three further observables to solve these issues in order to obtain accurate and precise pseudorange estimates. We show that

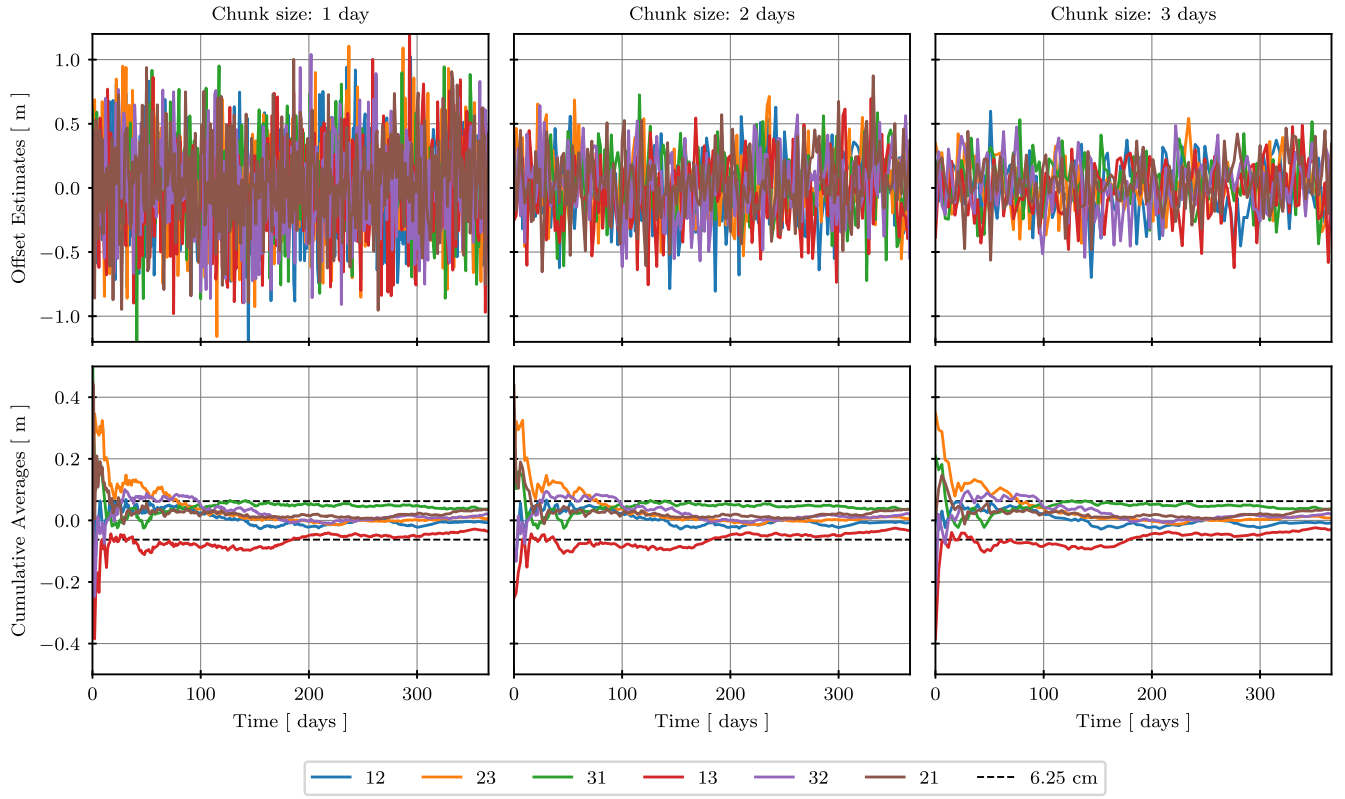

FIG. 10. We simulate one year of telemetry data with PRNR offsets on the order of 100 m. We divide this dataset into 1-day chunks (left plots), 2-day chunks (central plots), and 3-day chunks (right plots). We then we apply TDIR to each of these chunks in order to estimate the PRNR offsets. Upper plots: residual offset estimates in m for the different chunk sizes. Lower plots: residual offset estimates after cumulative averaging in m for the different chunk sizes. Dashed-black lines: half the SBR ambiguity.

both GOR and TDIR enable the resolution of the PRNR ambiguity. We investigate how onboard delays affect the pseudorange observables and propose an initial data treatment to compensate their effects (offsets and timestamping delays) based on an on-ground calibration of the onboard delays. We implement TDIR as a cross-check for the PRNR offset calibration. We use a Kalman filter to remove the white ranging noise combining PRNR and sideband range rates and apply the RFI beat notes to subtract the right-handed modulation noise. This leads to pseudorange estimates at subcentimeter accuracy. We show that in combination with phase anchor points they allow one to resolve the SBR ambiguities resulting in pseudorange estimates at submillimeter accuracy. Apart from that, we identify the delays that are to be applied in TDI in consideration of onboard delays. These are the pseudoranges in combination with onboard delays on both the emitter and the receiver side [see Eq. (13)].

TDI requires a ranging accuracy of about 10 m to suppress the laser frequency noise below the secondary noise levels [26]. While the main building blocks of the here presented RSF are necessary, the reached submillimeter ranging accuracy does not translate into a higher sensitivity for gravitational waves in the final output. Nevertheless, a better ranging accuracy is beneficial: The secondary noise levels might decrease during the decade until launch; in the case that the cavities perform below expectations, i.e., the encountered laser frequency noise is higher than expected, TDI needs a better ranging accuracy; also, in the context of next-generation space-based gravitational-wave missions, a better ranging accuracy might be advantageous.

From the economic perspective, it could be argued whether the onboard ranging system could be dropped in favor of TDIR. Hence, it must be emphasized that PRNR is the most reliable LISA pseudorange observable. After ambiguity resolution and offset correction, PRNR delivers a submeter ranging accuracy directly with the first sample. The TDIR estimator needs more than 1000 s of telemetry data to reach a similar accuracy [see Eq. (38)]. Hence, considering the possibility of data gaps, it is convenient to have PRNR as a direct pseudorange observable. Furthermore, PRNR is more robust than TDIR, which relies on the science data laser frequency noise being its signal. Not only the secondary noise sources, but also, e.g., gravitational-wave signals are noise to TDIR and degrade its performance. Finally, the PRN modulation has since long been a part of the LISA baseline architecture, as it serves another indisputable function: data transfer between the SC at 45–60 kbits s^{-1}. This requires some kind of digital phase modulation anyway. Implementing the

ranging function on top imposes only uncritical extra constraints on that modulation, i.e., synchronization of the digital codes to the SCET.

While we carefully investigate the effects of onboard delays in the ISI, we neglect them in the RFI and in the TMI. However, any differential delay between the laser frequency noise terms appearing in the ISI and in the RFI will cause residual laser frequency noise. Therefore, a follow-up study should investigate the effects of onboard delays for the full LISA interferometric system.

In the PRNR offset estimation via TDIR, we assume these offsets to be constant. In reality, however, they are expected to be slowly time varying. In a follow-up study, the PRNR offset estimation via TDIR should be extended to linearly time-varying PRNR offsets. The delay model for the TDIR estimator would then become

$$d_{ij}^{\hat{\tau}_i}(\tau) = \hat{R}_{ij}^{\hat{\tau}_i}(\tau) - (O_{ij}^0 + O_{ij}^1 \cdot \tau). \tag{64}$$

The TDIR estimator would now have to fit the six constants O_{ij}^0 and the six drifts O_{ij}^1. Tone-assisted TDIR [27] could be included in this study to reach a better accuracy.

Both the Kalman filter algorithm presented in Sec. IV B and the TDIR estimator presented in Sec. IV C are pseudorange estimators. A follow-up study could investigate whether their combination in a single estimator leads to better pseudorange estimates [28].

Furthermore, it would be interesting to include time-varying onboard delays and the associated SC monitors into the simulation. This would enable an inspection of the feasibility of the initial data treatment as proposed in Sec. IV.

Finally, the RSF could be included into the different INReP topologies. Apart from that, the algorithms could be applied to real data as, e.g., produced by the hexagon experiment [29,30].

ACKNOWLEDGMENTS

J. N. R. acknowledges the funding by the Deutsche Forschungsgemeinschaft (DFG, German Research Foundation) under Germany's Excellence Strategy within the Cluster of Excellence PhoenixD (EXC 2122, Project ID No. 390833453). Furthermore, he acknowledges the support by the IMPRS on Gravitational Wave Astronomy at the Max Planck Institute for Gravitational Physics in Hannover, Germany. This work is also supported by the Max Planck Society within the LEGACY ("Low-Frequency Gravitational-Wave Astronomy in Space") collaboration (M.IF.A.QOP18098). O. H. and A. H. acknowledge support from the Programme National GRAM of CNRS/INSU with INP and IN2P3 cofunded by CNES and from the Centre National d'Études Spatiales (CNES). The authors thank Miles Clark, Pascal Grafe, Waldemar Martens, and Peter Wolf for useful discussions. The study on PRNR offset estimation via TDIR was performed on the ATLAS cluster at AEI Hannover. The authors thank Carsten Aulbert and Henning Fehrmann for their support.

APPENDIX A: PSEUDORANGES IN TCB

The pseudorange can be expressed in TCB by writing the SCETs of receiving and emitting SC as functions of TCB evaluated at the events of reception and emission, respectively:

$$R_{ij}^t(t_{\mathrm{rec}}) = \hat{\tau}_i^t(t_{\mathrm{rec}}) - \hat{\tau}_j^t(t_{\mathrm{emit}}), \tag{A1}$$

where $\hat{\tau}_i^t$ denotes the SCET of SC i expressed as a function of TCB. The TCB of emission can be expressed as the difference between the TCB of reception and the light travel time from SC j to SC i, denoted by d_{ij}^t:

$$R_{ij}^t(t_{\mathrm{rec}}) = \hat{\tau}_i^t(t_{\mathrm{rec}}) - \hat{\tau}_j^t(t_{\mathrm{rec}} - d_{ij}^t(t_{\mathrm{rec}})). \tag{A2}$$

In the following, we drop the subscript; hence, t refers to the TCB of reception. The SCET can be expressed in terms of the SCET deviation from TCB:

$$\hat{\tau}_i^t(t) = t + \delta\hat{\tau}_i^t(t), \tag{A3}$$

which allows us to write Eq. (A2) as

$$R_{ij}^t(t) = \delta\hat{\tau}_i^t(t) + d_{ij}^t(t) - \delta\hat{\tau}_j^t(t - d_{ij}^t(t)). \tag{A4}$$

Expanding the SCET deviation of the emitting SC from TCB around the reception TCB yields

$$R_{ij}^t(t) = \delta\hat{\tau}_{ij}^t(t) + \left(1 + \delta\dot{\hat{\tau}}_j^t(t)\right) \cdot d_{ij}^t(t), \tag{A5}$$

$$\delta\hat{\tau}_{ij}^t(t) \coloneqq \delta\hat{\tau}_i^t(t) - \delta\hat{\tau}_j^t(t). \tag{A6}$$

Hence, in a global time frame like TCB, the pseudorange can be expressed in terms of the light travel time d_{ij}^t and the differential SCET offset $\delta\hat{\tau}_{ij}^t$.

APPENDIX B: SUBTRACTION OF RIGHT-HANDED MODULATION NOISE

Following the notation in [5], we express the RFI carrier and sideband beat notes in frequency:

$$\mathrm{RFI}_{ij}^{\hat{\tau}_i}(\tau) = \nu_{ik}^{\hat{\tau}_i}(\tau) - \nu_{ij}^{\hat{\tau}_i}(\tau), \tag{B1}$$

$$\mathrm{RFI}_{\mathrm{sb},ij}^{\hat{\tau}_i}(\tau) = \nu_{\mathrm{sb},ik}^{\hat{\tau}_i}(\tau) - \nu_{\mathrm{sb},ij}^{\hat{\tau}_i}(\tau), \tag{B2}$$

$$\nu_{\mathrm{sb},ij}^{\hat{\tau}_i}(\tau) = \nu_{ij}^{\hat{\tau}_i}(\tau) + \nu_{ij}^{\mathrm{m}} \cdot (1 + M_{ij}^{\hat{\tau}_i}). \tag{B3}$$

We combine these beat notes to form measurements of the right-handed modulation noise:

$$\begin{aligned}\Delta M_i^{\hat{\tau}_i} &:= \frac{\mathrm{RFI}_{ij}^{\hat{\tau}_i} - \mathrm{RFI}_{\mathrm{sb},ij}^{\hat{\tau}_i} + 1\ \mathrm{MHz}}{2} \\ &\quad - \frac{\mathrm{RFI}_{ik}^{\hat{\tau}_i} - \mathrm{RFI}_{\mathrm{sb},ik}^{\hat{\tau}_i} - 1\ \mathrm{MHz}}{2} \\ &= \nu_{ij}^{\mathrm{m}} \cdot M_{ij}^{\hat{\tau}_i} - \nu_{ik}^{\mathrm{m}} \cdot M_{ik}^{\hat{\tau}_i}, \end{aligned} \tag{B4}$$

i, j, and k being a cyclic permutation of 1, 2, and 3, respectively. We can now subtract the $\Delta M_i^{\hat{\tau}_i}$ measurements from the sideband range rates [Eq. (32)] to reduce the right-handed modulation noise. After that, we are limited by the one order of magnitude lower left-handed modulation noise:

$$\begin{aligned}\dot{\mathrm{SBR}}_{\mathrm{cor},ij}^{\hat{\tau}_i} &= \dot{\mathrm{SBR}}_{ij}^{\hat{\tau}_i} - \dot{\mathbf{D}}_{ij}^{\hat{\tau}_i} \cdot \Delta M_j^{\hat{\tau}_j}(\tau) \\ &= \nu_{ji}^{\mathrm{m}} \cdot \dot{R}_{ij}^{\hat{\tau}_i} + \nu_{ij}^{\mathrm{m}} \left(M_{ij}^{\hat{\tau}_i} - \dot{\mathbf{D}}_{ij}^{\hat{\tau}_i} \cdot M_{jk}^{\hat{\tau}_j}(\tau) \right), \end{aligned} \tag{B5a}$$

$$\begin{aligned}\dot{\mathrm{SBR}}_{\mathrm{cor},ik}^{\hat{\tau}_i} &= \dot{\mathrm{SBR}}_{ik}^{\hat{\tau}_i}(\tau) + \Delta M_i^{\hat{\tau}_i}(\tau) \\ &= \nu_{ki}^{\mathrm{m}} \cdot \dot{R}_{ik}^{\hat{\tau}_i} + \nu_{ki}^{\mathrm{m}} \left(M_{ij}^{\hat{\tau}_i} + \dot{\mathbf{D}}_{ik}^{\hat{\tau}_i} M_{ki}^{\hat{\tau}_k}(\tau) \right), \end{aligned} \tag{B5b}$$

i, j, and k being a cyclic permutation of 1, 2, and 3, respectively.

APPENDIX C: SOLAR WIND DISPERSION

The average solar wind particle density at the LISA orbit is about $10\mathrm{cm}^{-3}$. Hence, at the scales of optical wavelengths, the solar wind plasma can be treated as a free electron gas with the plasma frequency [31]

$$\nu_p^2 = \frac{n_e e^2}{4\pi^2 \epsilon_0 m_e} \approx 8 \times 10^8\ \mathrm{s}^{-2}, \tag{C1}$$

where n_e denotes the electron density, e the elementary charge, m_e the electron mass, and ϵ_0 the vacuum permittivity. Contributions from protons and ions can be neglected, as the plasma frequency is inversely proportional to the mass. We describe the refractive index of the solar wind plasma by the Appleton equation. Neglecting collisions and magnetic fields, it denotes

$$n(\nu) = \sqrt{1 - \left(\frac{\nu_p}{\nu}\right)^2}. \tag{C2}$$

In a dispersive medium, we need to distinguish between phase and group velocity. The phase velocity is given by

$$v_{\mathrm{p}}(\nu) = \frac{c}{n(\nu)} = \frac{c}{\sqrt{1 - (\frac{\nu_p}{\nu})^2}} \approx c \cdot \left(1 + \frac{1}{2}\frac{\nu_p^2}{\nu^2}\right), \tag{C3}$$

where we applied the expansion for $\nu \gg \nu_p$, as we consider optical frequencies. The product of group and phase velocity yields c^2. Consequently, the group velocity is

$$v_{\mathrm{g}}(\nu) = c \cdot n(\nu) = c \cdot \sqrt{1 - \left(\frac{\nu_p}{\nu}\right)^2} \approx c \cdot \left(1 - \frac{1}{2}\frac{\nu_p^2}{\nu^2}\right). \tag{C4}$$

The group and the phase delay for the interspacecraft signal propagation in LISA can now be expressed as

$$\Delta\tau_{\mathrm{g}}(\nu) = L\left(\frac{1}{c \cdot \sqrt{1 - (\frac{\nu_p}{\nu})^2}} - \frac{1}{c}\right) \approx \frac{L\nu_p^2}{2c} \cdot \frac{1}{\nu^2}, \tag{C5}$$

$$\Delta\tau_{\mathrm{p}}(\nu) = L\left(\frac{\sqrt{1 - (\frac{\nu_p}{\nu})^2}}{c} - \frac{1}{c}\right) \approx -\frac{L\nu_p^2}{2c} \cdot \frac{1}{\nu^2}, \tag{C6}$$

respectively, where $L = 2.5$ Gm denotes the LISA arm length. PRN and sideband signals propagate at the group velocity; hence, they are delayed by the group delay:

$$\Delta\tau_{\mathrm{g}}^{\mathrm{prn}} = \Delta\tau_{\mathrm{g}}(281\ \mathrm{THz} \pm 1\ \mathrm{MHz}) \approx 12.7\ \mathrm{pm}, \tag{C7}$$

$$\Delta\tau_{\mathrm{g}}^{\mathrm{sb}} = \Delta\tau_{\mathrm{g}}(281\ \mathrm{THz} \pm 2.4\ \mathrm{GHz}) \approx 12.7\ \mathrm{pm}. \tag{C8}$$

The phase delay is negative, because the phase velocity is bigger than c. Therefore, the laser phase is advanced with respect to a wave propagating in vacuum. For the LISA carrier, this phase advancement corresponds to

$$\Delta\tau_{\mathrm{p}}(281\ \mathrm{THz}) \approx -12.7\ \mathrm{pm}. \tag{C9}$$

[1] P. Amaro-Seoane, H. Audley, S. Babak, J. Baker, E. Barausse, P. Bender, E. Berti, P. Binetruy, M. Born, D. Bortoluzzi *et al.*, Laser interferometer space antenna, arXiv:1702.00786.

[2] O. Gerberding, B. Sheard, I. Bykov, J. Kullmann, J. J. E. Delgado, K. Danzmann, and G. Heinzel, Phasemeter core for intersatellite laser heterodyne interferometry: Modelling, simulations and experiments, Classical Quantum Gravity **30**, 235029 (2013).

[3] J. Armstrong, F. Estabrook, and M. Tinto, Time-delay interferometry for space-based gravitational wave searches, Astrophys. J. **527**, 814 (1999).

[4] M. Tinto, F. B. Estabrook, and J. Armstrong, Time-delay interferometry for LISA, Phys. Rev. D **65**, 082003 (2002).

[5] O. Hartwig, J.-B. Bayle, M. Staab, A. Hees, M. Lilley, and P. Wolf, Time-delay interferometry without clock synchronization, Phys. Rev. D **105**, 122008 (2022).

[6] J. J. Esteban, I. Bykov, A. F. G. Marín, G. Heinzel, and K. Danzmann, Optical ranging and data transfer development for LISA, J. Phys. Conf. Ser. **154**, 012025 (2009).

[7] J. J. Esteban, A. F. García, J. Eichholz, A. M. Peinado, I. Bykov, G. Heinzel, and K. Danzmann, Ranging and phase measurement for LISA, J. Phys. Conf. Ser. **228**, 012045 (2010).

[8] G. Heinzel, J. J. Esteban, S. Barke, M. Otto, Y. Wang, A. F. Garcia, and K. Danzmann, Auxiliary functions of the LISA laser link: Ranging, clock noise transfer and data communication, Classical Quantum Gravity **28**, 094008 (2011).

[9] O. Hartwig, Instrumental modelling and noise reduction algorithms for the laser interferometer space antenna, Ph.D. thesis, Leibniz Universitat Hannover, 2021, 10.15488/11372.

[10] Y. Wang, G. Heinzel, and K. Danzmann, First stage of LISA data processing: Clock synchronization and arm-length determination via a hybrid-extended Kalman filter, Phys. Rev. D **90**, 064016 (2014).

[11] A. Sutton, K. McKenzie, B. Ware, and D. A. Shaddock, Laser ranging and communications for LISA, Opt. Express **18**, 20759 (2010).

[12] M. Tinto, M. Vallisneri, and J. Armstrong, Time-delay interferometric ranging for space-borne gravitational-wave detectors, Phys. Rev. D **71**, 041101 (2005).

[13] J.-B. Bayle and O. Hartwig, Unified model for the LISA measurements and instrument simulations, Phys. Rev. D **107**, 083019 (2023).

[14] J.-B. Bayle, O. Hartwig, and M. Staab, Adapting time-delay interferometry for LISA data in frequency, Phys. Rev. D **104**, 023006 (2021).

[15] W. Brzozowski, D. Robertson, E. Fitzsimons, H. Ward, J. Keogh, A. Taylor, M. Milanova, M. Perreur-Lloyd, Z. Ali, A. Earle *et al.*, The LISA optical bench: An overview and engineering challenges, Space Telesc. Instrum. **12180**, 211 (2022).

[16] G. F. Barranco and G. Heinzel, A DC-coupled, HBT-based transimpedance amplifier for the LISA quadrant photoreceivers, IEEE Trans. Aerospace Electron. Syst. **57**, 2899 (2021).

[17] P. Euringer, G. Hechenblaikner, F. Soualle, and W. Fichter, Performance analysis of sequential carrier-and code-tracking receivers in the context of high-precision space-borne metrology systems, arXiv:2302.13819.

[18] S. Barke, *Inter-Spacecraft Frequency Distribution for Future Gravitational Wave Observatories* (Gottfried Wilhelm Leibniz Universität Hannover, Hannover, 2015).

[19] M. Otto, Time-delay interferometry simulations for the laser interferometer space antenna, Ph.D. thesis, Leibniz University, Hannover, 2015.

[20] W. Martens and E. Joffre, Trajectory design for the ESA LISA mission, Journal of the Astronautical Sciences **68**, 402 (2021).

[21] A. Hees, S. Bertone, and C. Le Poncin-Lafitte, Relativistic formulation of coordinate light time, doppler, and astrometric observables up to the second post-Minkowskian order, Phys. Rev. D **89**, 064045 (2014).

[22] J.-B. Bayle, O. Hartwig, and M. Staab, *LISA Instrument* (Zenodo, 2021), 10.5281/zenodo.6447390.

[23] J.-B. Bayle, O. Hartwig, A. Petiteau, and M. Lilley, LISANode (2022).

[24] J.-B. Bayle, A. Hees, M. Lilley, C. Le Poncin-Lafitte, W. Martens, and E. Joffre, LISA Orbits (2022).

[25] M. Staab, J.-B. Bayle, and O. Hartwig, *PyTDI* (Zenodo, 2021), 10.5281/zenodo.6351736.

[26] M. Tinto, D. A. Shaddock, J. Sylvestre, and J. Armstrong, Implementation of time-delay interferometry for LISA, Phys. Rev. D **67**, 122003 (2003).

[27] S. P. Francis, D. A. Shaddock, A. J. Sutton, G. De Vine, B. Ware, R. E. Spero, W. M. Klipstein, and K. McKenzie, Tone-assisted time delay interferometry on GRACE follow-on, Phys. Rev. D **92**, 012005 (2015).

[28] Q. Baghi, J. G. Baker, J. Slutsky, and J. I. Thorpe, Fully data-driven time-delay interferometry with time-varying delays, Ann. Phys. (Berlin) 2200447 (2023).10.1002/andp.202200447

[29] K. Yamamoto, C. Vorndamme, O. Hartwig, M. Staab, T. S. Schwarze, and G. Heinzel, Experimental verification of intersatellite clock synchronization at LISA performance levels, Phys. Rev. D **105**, 042009 (2022).

[30] T. S. Schwarze, G. F. Barranco, D. Penkert, M. Kaufer, O. Gerberding, and G. Heinzel, Picometer-stable hexagonal optical bench to verify LISA phase extraction linearity and precision, Phys. Rev. Lett. **122**, 081104 (2019).

[31] A. Smetana, Background for gravitational wave signal at LISA from refractive index of solar wind plasma, Mon. Not. R. Astron. Soc. **499**, L77 (2020).